STUDY OF MOLECULAR VIBRATIONS AND SPECTROSCOPY OF NANO CAVITIES

Submitted on 20 March 2020
Masters' Thesis
Research Lab: Laboratory of Quantum Nano-Optics
École Polytechnique Fédérale de Lausanne

Sachin Verlekar

Thesis Advisors:

Prof Christophe Galland, Thesis Supervisor
Prof TS Mahesh, TAC

Lausanne, EPFL, 2020

Nobody ever figures out what life is all about,
and it doesn't matter.
Explore the world.
Nearly everything is really interesting
if you go into it deeply enough.
— Richard Feynman

To my parents and teachers...

Certificate

This is to certify that this dissertation entitled " STUDY OF MOLECULAR VIBRATIONS AND SPECTROSCOPY OF NANO CAVITIES " towards the partial fulfilment of the BS-MS dual degree programme at the Indian Institute of Science Education and Research, Pune represents study/work carried out by Sachin Verlekar at École polytechnique fédérale de Lausanne (EPFL) under the supervision of Christophe Galland, SNSF-Funded Professor, during the academic year 2019-2020.

Student: 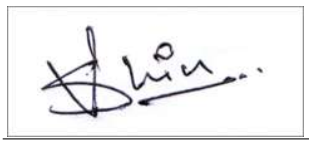

Sachin Verlekar

Supervisor: 

Prof. Christophe Galland

Declaration

I hereby declare that the matter embodied in the report entitled " STUDY OF MOLECULAR VIBRATIONS AND SPECTROSCOPY OF NANO CAVITIES " are the results of the work carried out by me at the Department of Physics, École polytechnique fédérale de Lausanne, under the supervision of Prof. Christophe Galland and the same has not been submitted elsewhere for any other degree.

Student: 

Sachin Verlekar

Supervisor: 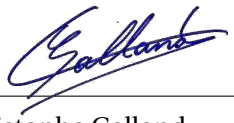

Prof. Christophe Galland

Acknowledgements

I wish to express my sincere gratitude for my supervisor, Professor Christophe Galland, whose vision and ever-present guidance through each step of the project was vital in ensuring not only that progress was made, but also that I learnt a lot while doing so. The timely evaluation and feedback from Professor T.S. Mahesh was key throughout the journey of this project. I would like to thank all the members of the LQNO research group for their stimulating discussions, guidance and help with a myriad of specific questions in the lab. This project could be envisioned due to the support of my university, IISER Pune, which provided the option of pursuing a Masters' Thesis project at EPFL, where the Masters' Thesis project was hosted. I am indebted to all my friends and family members, without whose unwavering support and undiminished enthusiasm this project would not have been possible.

April 4, 2020 S. V.

Abstract

The concept of Molecular Optomechanics was recently proposed, motivated by the fact that molecular vibrations behave as mechanical oscillators in their quantum ground state at room temperature, and that they can be coupled to plasmonic nanocavities to realise optomechanical systems. This thesis explores with theoretical and experimental works new topics in molecular optomechanics.

The first part of this Thesis develops a quantum model for anharmonic coupling between two vibrational modes of a molecule and computes the expected time evolution of vibrational populations after preparation of the system in a phonon-number state. This work is inspired by recent experiments in the host group demonstrating a technique to excite the first Fock state of a phonon in a crystal, and lays the basis for future experimental work on molecular systems.

Apart from studying the vibrational dynamics itself, molecular optomechanics also aims at engineering the coupling between localised plasmons and Raman-active molecular vibrations. To this aim, it is essential to perform high precision spectroscopy of both Stokes and anti-Stokes sideband with a broadly tunable excitation source. The second and third part of this Thesis focus on the design and implementation of such a setup.

In the second part, I present the design and optimisation, with a ray tracing software, and then the fabrication and assembly of a tunable notch spectral filter, which allows blocking the reflected laser light from the sample under study while collecting both Stokes and anti-Stokes Raman sidebands. Characterisation of the device confirms that the extinction ratio is suitable for Raman spectroscopy without the need of additional interference filters, greatly simplifying tunable excitation and detection.

Finally, the third part of the Thesis describes the design, construction and first operational outcome of a cryogenic microscope for multimodal spectroscopy, allowing simultaneous excitation of plasmonic nanocavities with different wavelengths. This setup was instrumental in revealing hitherto elusive fluctuations of metal-induced luminescence, while monitoring the stability of the vibrational Raman signal.

Overall, this Thesis provides important contribution to our understanding of light-matter interactions and vibrational dynamics in the context of molecular optomechanics with plasmonic nanocavities.

Key words: Intermode vibrational coupling, Tunable Notch filter, Plasmonic blinking

Contents

List of Figures

1 Molecular simulations

1.1 Introduction

It has been recently shown by the host group that it is possible to prepare the first excited Fock state (i.e., a single quantum of energy) of a vibrational mode of a crystal at room temperature. After exciting a bulk diamond with a 100 femtosecond laser pulse we can detect a scattered photon at lower energy - a so-called Stokes photon - which is heralding (announcing) the creation of a single quantized excitation in the 40 THz Raman-active internal vibrational mode of diamond. When we detect a single Stokes photon, we know that the vibration was prepared in the Fock state $|1\rangle$ with about 98.5% probability. This was verified by reading out the state using a second, different colored, ultrashort laser pulse. The anti-Stokes Raman signal, which is created only when a vibrational excitation is already present in the diamond, is then subjected to a Hanbury-Brown-Twiss intensity correlation measurement, revealing the sub-Poisson (and therefore non-classical) statistics of the vibrational mode. [1]

Interestingly, the experimental method is general and is to be extended to more complex systems having multiple phonon modes exhibit rich and complex couplings between different modes. The experimental and theoretical investigations undertaken are to progress towards an understanding of the expected correlations and their time evolution in such multi-mode systems. I am trying to understand, through theory and simulations, the effects of anharmonic intermode coupling between vibrational modes on the dynamics of populations and quantum correlations.

1.2 Methods

An important theoretical tool for this aspect is Canonical Van Vleck Perturbation Theory (CVPT). CVPT is a powerful form of quantum mechanical perturbation theory based on using the operator form of the Hamiltonian and transforming it into a more intuitive form through successive canonical transformations. For our purposes, the 'desired form' would be a block diagonal form, where each block consists of the energy levels that are interconnected by

resonances. The advantage of CVPT lies in the fact that we can explicitly deduce the relevant operators and coefficients in the Hamiltonian to describe the aforementioned couplings. The final form of the Hamiltonian thus obtained is ideal to use for numerical simulations. To simulate these systems, QuTiP (Quantum Toolbox in Python) was used. We will first start with a brief introduction of the harmonic approximation and normal modes followed by a description of CVPT and it's implementation using QuTiP.

1.2.1 Harmonic approximation and normal modes

To describe molecular vibrations using normal modes, we start with the classical Hamiltonian describing N atoms using the cartesian coordinates x_i :

$$H = \sum_{i=1}^{3N} \frac{m_i}{2} \left(\frac{\mathrm{d}x_i}{\mathrm{d}t} \right)^2 + V(x_1, \ldots, x_{3N})$$

and we assume that the potential has a well-defined minimum (defined by equilibrium coordinates x_i^e). For convenience, we introduce the mass-weighted coordinates and Taylor expand the potential around the minimum :

$$q_i = \sqrt{m_i} \Delta x_i = \sqrt{m_i} \left(x_i - x_i^{\mathrm{e}} \right)$$
$$V = V_0 + \sum_{i=1}^{3N} \left(\frac{\partial V}{\partial q_i} \right)_0 q_i + \frac{1}{2} \sum_{i=1}^{3N} \sum_{j=1}^{3N} \left(\frac{\partial^2 V}{\partial q_i \partial q_j} \right)_0 q_i q_j + \cdots$$

On neglecting the higher-order terms in the expansion, the classical Hamiltonian takes the form :

$$H = T + \frac{1}{2} \sum_{i=1}^{3N} \sum_{j=1}^{3N} F_{ij} q_i q_j \qquad T = \frac{1}{2} \sum_{i=1}^{3N} \left(\frac{\mathrm{d}q_i}{\mathrm{d}t} \right)^2 \qquad F_{ij} = \left(\frac{\partial^2 V}{\partial q_i \partial q_j} \right)_0$$

We can then make a transformation to the set of normal coordinates Q_k:

$$Q_k = \sum_{i=1}^{3N} L_{ik} q_i$$

where $\mathbf{L}$ is an orthogonal transformation with $\mathbf{L}^{-1} = \mathbf{L}^T$. The expression for the kinetic and potential energy become :

$$T = \frac{1}{2} \sum_{i=1}^{3N} \left(\frac{\mathrm{d}Q_i}{\mathrm{d}t} \right)^2 \qquad V = \frac{1}{2} \sum_{k=1}^{3N} \lambda_k Q_k^2$$

where λ_k are functions of the force constants F_{ij}. Thus, the total classical Hamiltonian can be

written as a sum over classical hamiltonians for each normal mode :

$$H = \sum_{i=1}^{3N} H_i \left(Q_i, \frac{\mathrm{d}Q_i}{\mathrm{d}t} \right)$$

Translating this to quantum mechanics and solving the corresponding Schrodinger equation one obtains energy levels $E_{\mathrm{n}_1,\mathrm{n}_2,\mathrm{n}_3\ldots}$ and wave functions $\Psi_{\mathrm{n}_1,\mathrm{n}_2,\mathrm{n}_3\ldots}$

$$E_{\mathrm{n}_1,\mathrm{n}_2,\mathrm{n}_3\ldots} = \sum_{i=1}^{3N} E_{\mathrm{n}_i}$$

$$\Psi_{n_1,n_2,n_3\ldots}(Q_1,Q_2,Q_3,\ldots) = \prod_{i=1}^{3N} \Psi_{n_i}(Q_i)$$

For the quantum energy levels of the i^{th} mode,

$$E_{\mathrm{v}_i} = \left(\mathrm{v}_i + \frac{1}{2} \right) h v_i \qquad\qquad v_i = \frac{1}{2\pi}\sqrt{\lambda_i} = \frac{1}{2\pi}\sqrt{\frac{f_i}{\mu_i}}$$

where f_i and μ_i are the generalised force constants and generalised reduced masses respectively.

1.2.2 Anharmonicity

In real polyatomic molecules, anharmonicity leads to much more complex spectra and dynamics than suggested by the harmonic approximation. The effect of these can be incorporated by introducing higher order terms in the potential:

$$\begin{aligned} V(Q) =& \frac{1}{2}\sum_k \lambda_k Q_k^2 + \frac{1}{6}\sum_{k,l,m} \Phi_{k,l,m} Q_k Q_l Q_m \\ &+ \frac{1}{24}\sum_{k,l,m,n} \Phi_{k,l,m,n} Q_k Q_l Q_m Q_n + \cdots \end{aligned}$$

If the aforementioned Taylor expansion converges rapidly and there are no "resonances" (described below), other than degenerate vibrations, the anharmonic term can be written using perturbation theory as:

$$\begin{aligned} \frac{E_{\mathrm{n}_1\mathrm{n}_2\ldots}}{hc} =& G(\mathrm{n}_1,\mathrm{n}_2,\ldots) \\ =& \sum_k \omega_k \left(\mathrm{v}_k + \frac{1}{2} \right) \\ &+ \sum_{k\geq l} x_{kl} \left(\mathrm{n}_k + \frac{1}{2} \right) \left(\mathrm{n}_l + \frac{1}{2} \right) + \cdots \end{aligned}$$

where the harmonic frequencies and higher order constants can be related to more fundamental properties of the molecule such as force constants. However, these expressions fail if

there is an anharmonic resonance interaction between states lying close together in energy.

1.2.3 Preliminary description of two-level resonance

Let us consider the case where in the harmonic approximation, two energy levels are very close together in energy (E_i^0 and E_n^0). The higher order (anharmonic) term can be accounted locally for these two energy levels by calculating the coupling between the transition matrix element between the two close-lying levels.

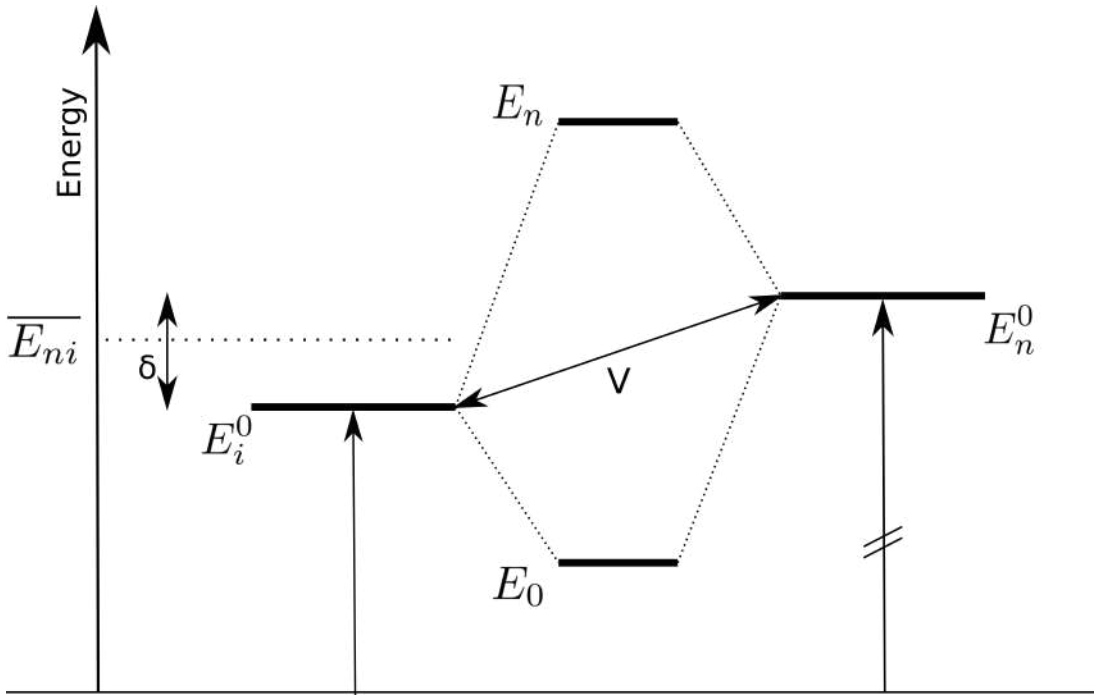

Figure 1.1 – Schematic for two energy levels in "resonance" is shown along with the energy levels formed subsequently.

$$V_{in} = \left\langle E_i^0 \right| \hat{V} \left| E_n^0 \right\rangle$$

We define the two levels to be in 'resonance' if the magnitude of the coupling $|V_{in}|$ is similar to the zero-order energy separation of the levels.

$$|V_{in}| \approx |E_i^0 - E_n^0| = |\delta|$$

In this scenario, the Hamiltonian takes the form :

$$\boldsymbol{H}_{\text{eff}} = \begin{pmatrix} E_i^0 & W_{in} \\ W_{ni} & E_n^0 \end{pmatrix} = \begin{pmatrix} H_{11} & H_{12} \\ H_{21} & H_{22} \end{pmatrix}$$

which is a Hermitian matrix. We define $|V_{ni}|^2 = |V_{in}|^2 = V^2$. The eigenvalues of the Hamiltonian are :

$$E_{i,n} = \overline{E_{ni}} \pm \frac{1}{2}\sqrt{4W^2 + \delta^2} \qquad \overline{E_{ni}} = \frac{\left(E_i^0 + E_n^0\right)}{2} = \frac{(E_i + E_n)}{2}$$

with the eigenfunctions

$$\psi_i = a\psi_i^0 - b\psi_n^0 \qquad \psi_n = b\psi_i^0 + a\psi_n^0$$

with the coefficients given by :

$$a = \left(\frac{\sqrt{4W^2+\delta^2}+\delta}{2\sqrt{4W^2+\delta^2}}\right)^{1/2} \qquad b = \left(\frac{\sqrt{4W^2+\delta^2}-\delta}{2\sqrt{4W^2+\delta^2}}\right)^{1/2}$$

Note that in the regime $\delta^2 >> 4V^2$, we have,

$$E_{i,n} \approx \overline{E_{ni}} \pm \left(\frac{\delta}{2} + \frac{V^2}{\delta}\right)$$

which implies that $E_i \rightarrow E_i^0$ and $E_n \rightarrow E_n^0$ with $E_n^0 - E_i^0 = \delta$. This justifies neglecting non-resonant levels as the effect on them is very small. In the case of a Fermi resonance, E_i corresponds to the first excited state of one vibration ($n_1 = 1$, $n_2 = 0$ and all other $n_k = 0$) and E_n to an overtone of a second vibration ($n_1 = 0$, $n_2 = 2$ and all other $n_k = 0$). Another type of resonance is the 'Darling-Dennison' resonance, where two quanta are exchanged between two modes having different symmetry but similar energy. E_i corresponds to ($n_1 = 2$, $n_2 = 0$) and E_n to ($n_1 = 0$, $n_2 = 2$). These are the resonances which lead to intramolecular coupling between vibrational modes. An extensive discussion can be found in [2].

1.2.4 Canonical Van Vleck Perturbation Theory (CVPT)

The spectroscopic Hamiltonian and resonances

In order to fully describe a molecule quantum mechanically, including all resonances, one would need the full expression for the potential energy surface (PES) due to all the constituents of the molecule. However, even for triatomic molecules, it is very heavy computationally to do so. And for larger polyatomic molecules, crystals etc. it is still a challenge to compute the PES ab initio even with the current computational resources. Thus, we need other ways to delve deeper in the intramolecular interactions. One of these is the spectroscopic Hamiltonian.

As described very well in [3], although there has been a lot of progress in the field of ab initio methods, the computational burden for obtaining experimental accuracy in spectroscopy and chemical dynamics is huge. Thus, the idea is to extract effective hamiltonians using perturbative or algebraic methods and then fit them to ab-initio or experimental spectra. One such method is Vleck perturbation theory [4] which is also covered very well in another

reference [5]. This is a perturbation theory carried out using the creation and annihilation operators in place of the matrix elements used in the normal perturbation theory.

The spectroscopic hamiltonians are written as a sum of two types of terms. Diagonal terms representing the energy and non-diagonal terms representing the 'resonances'. These are the terms we would be interested in for studying the intermode coupling between the various normal modes.

$$H = H_{\mathrm{D}} + H_{\mathrm{R}} \text{ where,}$$

$$H_{\mathrm{D}} = \sum_i \omega_i I_i + \sum_{i,k} x_{ik} I_i I_k + \sum_{i,k,m} y_{ikm} I_i I_{km} + \ldots$$

In this case, H_{D} or the terms on the right represent the diagonal matrix elements in a basis set expansion of the i^{th} **harmonic oscillator eigenfunctions**. The constants $\left(x_{ik}, y_{ikm}\right)$ are fitten to experimental data and,

$$I_i = \frac{1}{2}\left(p_i^2 + q_i^2\right) = a_i^\dagger a_i + \frac{d_i}{2} = n_i + \frac{d_i}{2}$$

where d_i denotes the degeneracy. For example, in a linear molecule, $d_i = 1$ for stretching modes but $d_i = 2$ for bending modes. The more interesting part for us, the non-diagonal part, is a sum of non-linear resonances :

$$H_{\mathrm{R}} = \sum_{\mathrm{R}} c_{\mathrm{R}} V_{\mathrm{R}}\left(a_i, a_i^\dagger\right)$$

A '**resonance**' between N vibrational modes implies the relation :

$$m_1\omega_1 + m_2\omega_2 + \ldots + m_{\mathrm{N}}\omega_{\mathrm{N}} = m \bullet \omega \approx 0$$

where $m_i \in \mathbb{Z}$ and ω_i are the frequencies of the modes involved. Some examples of this are :

Fermi resonance between a stretching and a bending oscillation ($\omega_{\mathrm{s}} - 2\omega_{\mathrm{b}} \approx 0$). The corresponding resonance term is written as: $V_{\mathrm{F}} = c_{\mathrm{F}}\left(a_{\mathrm{b}} a_{\mathrm{b}} a_{\mathrm{s}}^\dagger + a_{\mathrm{b}}^\dagger a_{\mathrm{b}}^\dagger a_{\mathrm{s}}\right)$

Similarly, for a Darling-Dennison coupling between a symmetric and anti-symmetric stretch ($2\omega_{\mathrm{s}} - 2\omega_{\mathrm{a}} \approx 0$) , the resonance term is : $V_{\mathrm{DD}} = c_{\mathrm{DD}}\left(a_{\mathrm{s}}^\dagger a_{\mathrm{s}}^\dagger a_{\mathrm{a}} a_{\mathrm{a}} + a_{\mathrm{s}} a_{\mathrm{s}} a_{\mathrm{a}}^\dagger a_{\mathrm{a}}^\dagger\right)$

CVPT formalism

Canonical perturbation methods rely on the principle that under a unitary transformation (U), the energy spectrum of a Hamiltonian (H) remains unchanged. The transformed Hamiltonian (K) is given by :

$$K = UHU^{-1}$$

The wavefunctions ψ of H and ϕ of K are related by:

$$\phi = U\psi$$

In the canonical perturbation theory (CPT) formalism, we aim to find the 'best' set of canonical coordinates through a series of unitary transformations. In the case that we are interested, the 'best' set of conjugate coordinates would be the ones in which the Hamiltonian is block-diagonal with the blocks corresponding to various **polyads** (this will be described later). The most preferred form of U is :

$$U = \exp(S) = \sum_{k=0}^{\infty} \frac{1}{k!} S^k = 1 + S + \frac{S^2}{2} + \frac{S^3}{6} + \ldots$$

where S is anti-Hermitian. This choice is made bacause :

- It gives real coefficients for the entire computed series (described below)
- The inverse transformation is $U^{-1} = \exp(-S)$
- For small S, we get the operator to be 1 + *corrections*

Thus, the general perturbation procedure consists of finding a series of anti-hermitian operators $S^{(k)}$ such that :

$$H^{(1)} = \exp\left(S^{(1)}\right) H^{(0)} \exp\left(-S^{(1)}\right)$$

$$H^{(2)} = \exp\left(S^{(2)}\right) H^{(1)} \exp\left(-S^{(2)}\right)$$

$$\vdots$$

$$H^{(s)} = \exp\left(S^{(s)}\right) H^{(s-1)} \exp\left(-S^{(s)}\right)$$

$$\vdots$$

where $H^{(0)} = H$ is the initial Hamiltonian and s represents the perturbation order. The Hamiltonian at order s can also be written as :

$$H^{(s)} = H^{(s-1)} + \left[S^{(s)}, H^{(s-1)}\right] + \frac{1}{2!}\left[S^{(s)}, \left[S^{(s)}, H^{(s-1)}\right]\right] + \frac{1}{3!}\left[S^{(s)}, \left[S^{(s)}, H^{(s-1)}\right]\right] + \ldots$$

which is the BCH formula. The flexibility of CPT lies in the choice of the operator $S^{(s)}$ at each order of the perturbation. To guide the choice of $H^{(s)}$, we introduce a book-keeping parameter λ (which is set to 1 in the end). Each interpolation Hamiltonian $H^{(s)}$ is expanded in the form:

$$H^{(s)} = \sum_k \lambda^k H^{(s,k)}$$

and the transformation at order s can be written as:

$$H^{(s)} = \exp\left(\lambda^s S^{(s)}\right) H^{(s-1)} \exp\left(-\lambda^s S^{(s)}\right)$$

Then, expanding according to the BCH formula and comparing orders of λ on both sides we find :

- if $k < s, H^{(s,k)} = H^{(s-1,k)}$: Thus, the transformation at order s does not affect the lower order terms.
- if $k = s, H^{(s,s)} = H^{(s-1,s)} + [S^s, H^{(0,0)}]$: This is used to choose the operator $S^{(s)}$ by requiring the second term to cancel out the physically unimportant terms.
- if $k > s, H^{(s,k)} = H^{(s-1,k)} + \sum_m \frac{1}{n!}[S^{(s)}, \ldots [S^{(s)}, H^{(s-1,m)}] \ldots]$

The sum of the physically important terms upto order s is called the perturbative Hamiltonian up to order s and is given by :

$$K^{(s)} = \sum_{k=0}^{s} H^{(s,k)} = \sum_{k=0}^{s} H^{(k,k)}$$

Use of CVPT in studying molecular vibrations and resonances

For studying molecular spectra / couplings, it is best to write the spectroscopic Hamiltonian in terms of creation and annihilation operators (CAO). As described in the previous section, The canonical transformations can be reduced to adding certain terms to the Hamiltonian arranged by the orders of perturbation theory, $H = H_0 + H_1 + H_2 = \Sigma H_K$.

The S_K operator needed for cancellation of the non-resonant off-diagonal terms after the final summations can be obtained using the following formula:

$$S = -\mathrm{i} \sum_j h_j \left(\sum_{l=1}^{M} \left(m_{jl} - n_{jl} \right) \omega_l \right)^{-1} \prod_{l=1}^{M} \left(a_l^\dagger \right)^{m_j} (a_l)^{n_{jl}}$$

and the following equality is useful in evaluating the commutators$[S_K, H_L]$:

$$\left(a^\dagger\right)^k a^l \left(a^\dagger\right)^m (a)^n = \left(a^\dagger\right)^{k+m} (a)^{l+n} \quad + \sum_{i=1}^{\min(l,m)} \left[\left(\frac{1}{i!} \prod_{j=0}^{i-1} (l-j)(m-j) \right) \left(a^\dagger\right)^{k+m-i} (a)^{l+n-i} \right]$$

The resonance terms are recognised by abnormally large values of a dimensionless quantity Ω_k while the value of the denominator Δ_k does not exceed a certain limit $\Delta^\dagger$

$$\Omega_k = h_k \left(\sum_{l=1}^{M} (m_{kl} - n_{kl})\, \omega_l \right)^{-1} \quad |\Omega_k| > \Omega^\dagger \qquad \Delta_k = \left(\sum_{l=1}^{M} (m_{kl} - n_{kl})\, \omega_l \right)^{-1} < \Delta^\dagger$$

But how to decide the threshold for categorizing the terms as "abnormally large" ? There are two ways:

- Evaluation of quantities of Ω_k for well-studied cases.
- A systematic choice of resonance criterion is directly linked with the concept of vibrational polyad quantum number. For a correct choice of resonance operators, the Hamiltonian matrix is canonically transformed into a block diagonal form. The consequence is that resonance couplings are confined to blocks and no interblock couplings occur. This is what was hinted at earlier about the connection between the 'best' form of the Hamiltonian and polyads.

Interestingly, the S_K operators can be used to transform any scalar molecular property that is expanded around the equilibrium point in a Taylor series. Thus, the components of the dipole moment, components of Raman tensor etc. can be transformed. This enables us to find the Raman spectra with the inclusion of anharmonicities and intermode couplings and make spectral assignments.

In this manner, given a particular molecule with the corresponding 0^{th} order eigenfrequencies, it is possible to find the appropriate resonance operators and other molecular properties incorporating these resonances and anharmonicities.

1.3 Results

To get an intuition of the effect of intramode couplings, simpler simulations were made

1.3.1 Two modes with Fermi resonance and DD coupling

$H = c_{DD}(a_1^\dagger a_1^\dagger a_2 a_2 + a_2^\dagger a_2^\dagger a_1 a_1)$ for DD resonance and
$H = c_F(a_1^\dagger a_2 a_2 + a_2^\dagger a_2^\dagger a_1)$ for Fermi resonance

here the $a_i, i \in 1,2$ correspond to the annihilation operators corresponding to the two vibrational modes. The vibrational states are initialised in the Fock states with the occupation numbers given in the titles of the graphs.

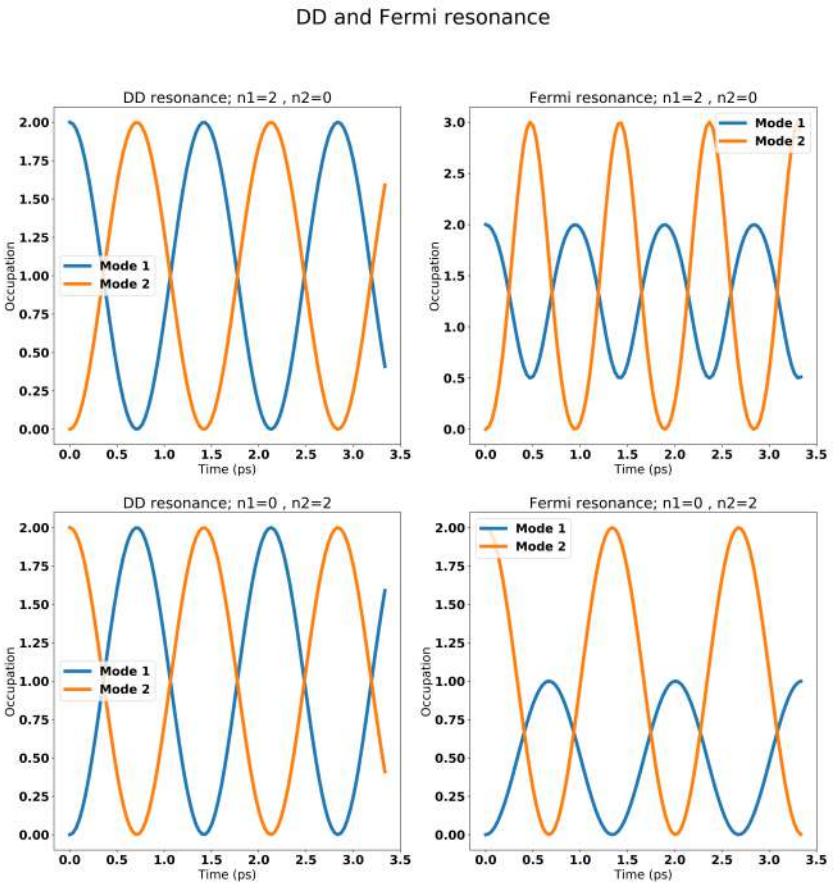

Figure 1.2 – Two normal modes coupled by DD and Fermi resonance are simulated. In the absence of any dephasing, we clearly see the periodic exchange of population between the two states.

We then see the effect of the dephasing on the vibrational dynamics. We consider a bath made of harmonic oscillators which can be modelled by the following collapse operators in the Master equation :

$$\sqrt{\kappa(1+n^{th})}a_i \qquad\qquad \sqrt{kn^{th}}a_i^{\dagger}$$

where k represents the coupling to the heat bath and n^{th} represents the average thermal occupation of the heat bath. In our simulations we consider $\kappa = 70$ and $n^{th} = 0.0015$.

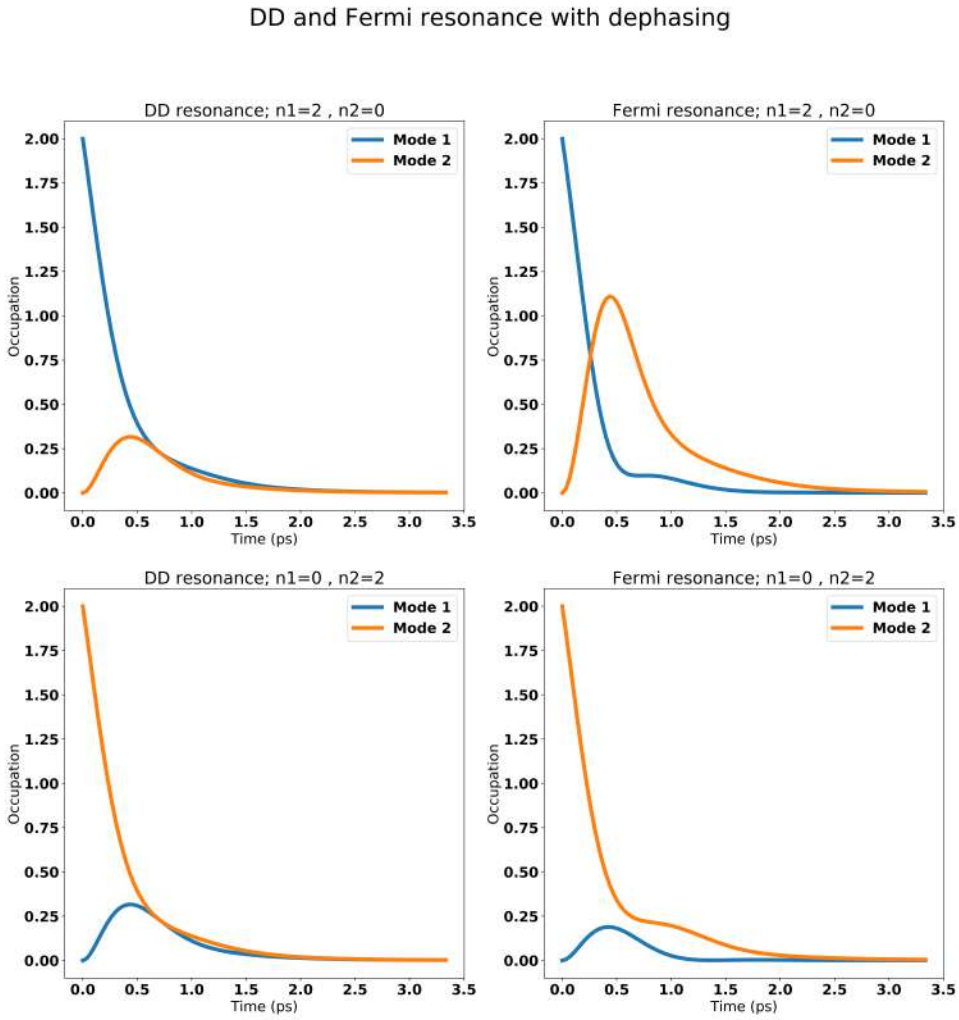

Figure 1.3 – When we add the dephasing terms, we still see a population transfer between states followed by a decay due to the thermal bath.

1.3.2 Simulation for water molecule (H_20)

The normal modes of vibration in a water molecule are shown below schematically :

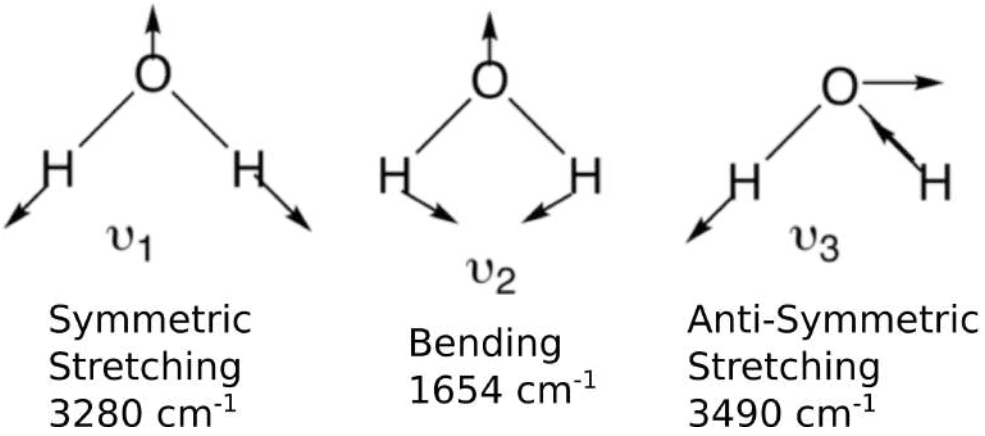

Figure 1.4 – The Normal modes of vibration of a water molecule are shown along with the corresponding vibrational frequencies

Using the theory of CVPT as described in the previous section, starting from the Normal mode frequencies, we can find the corresponding higher order resonances and the relevant coefficients in the Hamiltonian. The explicit calculation for water molecule has been done previously. From the analysis performed, we get the following resonance operators along with their corresponding coefficients [5]:

Resonance	H-coefficient (cm^{-1})	Resonance operator
Fermi Resonance	55.34	$a_b a_b a_s^\dagger + a_b^\dagger a_b^\dagger a_s$
Darling-Dennison Resonance	-36.92	$a_s^\dagger a_s^\dagger a_a a_a + a_s a_s a_a^\dagger a_a^\dagger$

Using these parameters, simulations were carried out in Qutip. Similar to the previous simulations, we consider the system to be coupled to a thermal bath of harmonic oscillators with $n^{th} = 0.0015$ and $\kappa = 70$ The results are summarised in the figures shown below. Note that the values of κ (coupling to the bath environment) and n^{th} (average occupation of the thermal bath) were chosen arbitrarily and can be fixed using known experimental variables in the future. We first show a schematic of the initial states followed by the simulation results:

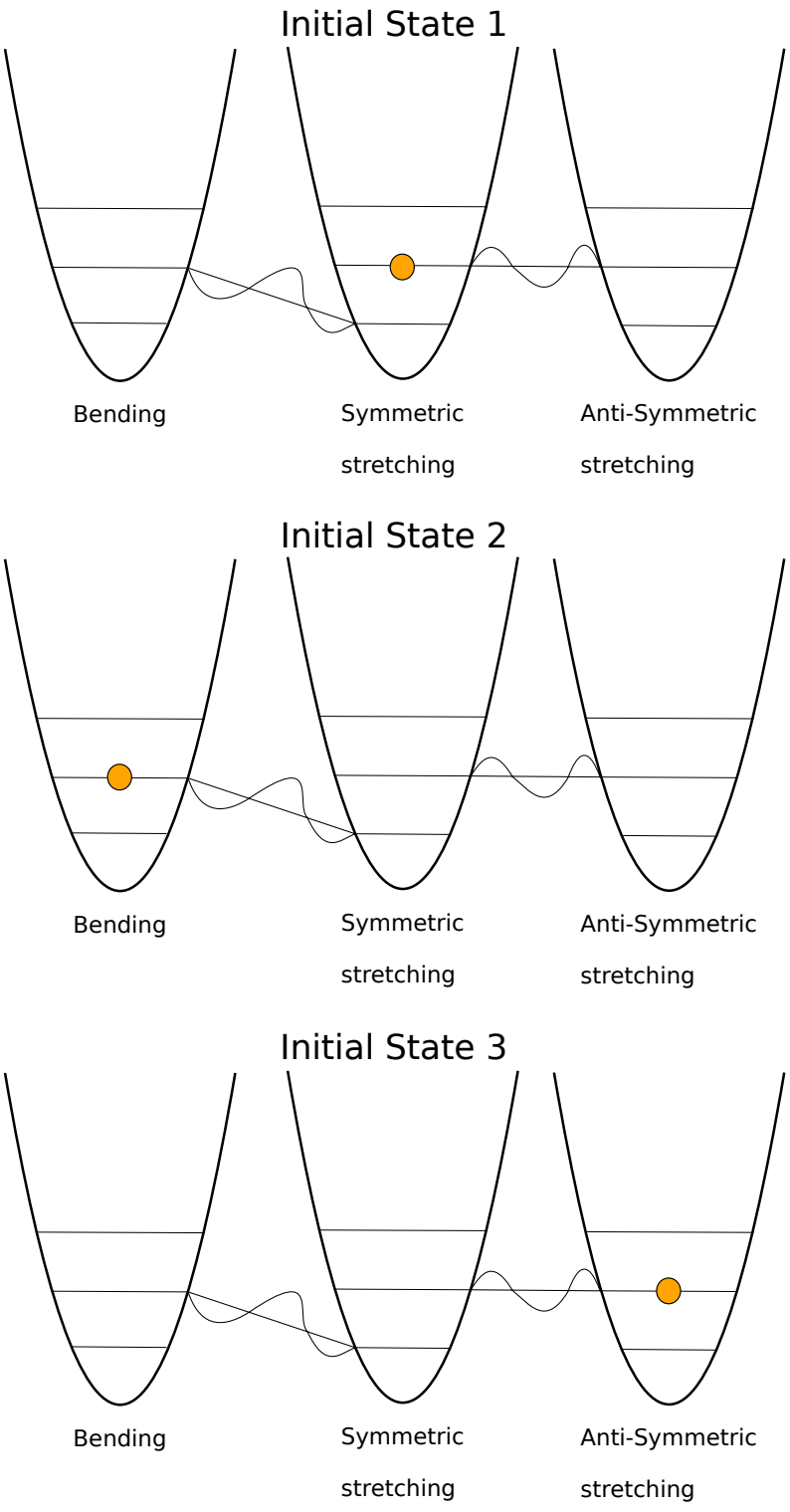

Figure 1.5 – A schematic for the initial states is shown along with the inter-mode couplings present in the water molecule.

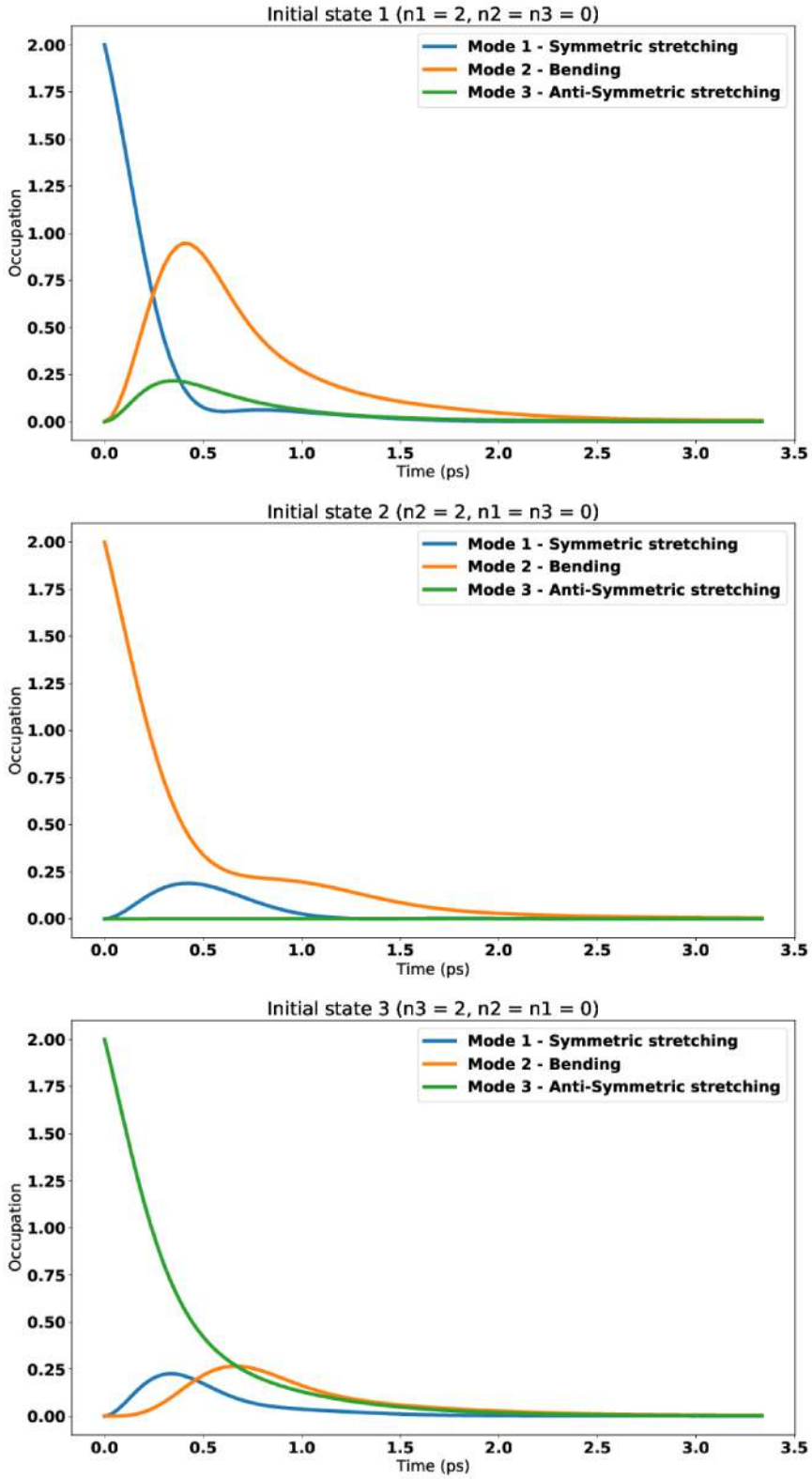

Figure 1.6 – The result of the Qutip simulations performed on the vibrational modes of water are shown. These shown the dynamics of population transfer under various initial conditions.

To understand the results, it is useful to recollect the couplings in terms of exchange of quanta of vibration.

Resonance	Coupling
Fermi Resonance	Bending : Symmetric Stretch (2:1) coupling
Darling-Dennison Coupling	Asymmetric Stretch : Symmetric stretch (2:2) coupling

In the first figure, we start with two quanta of excitation in the symmetric stretch mode, which is coupled to the asymmetric stretching $(2:2)$ as well as bending mode $(1:2)$. Thus, we clearly see the population transfer to both these modes. In case of the second figure, we see population transfer from the bending mode to the symmetric stretch mode. However, since it is coupled to the symmetric stretch mode $2:1$, there is no population transfer to the anti-symmetric mode from the symmetric mode. In the final figure, we see population transfer from the Anti-symmetric stretch to the Symmetric stretch mode which in turn transfers it to the bending mode. The timescales predicted by the simulation can be accessed by the ultrafast laser setup currently employed by the group. Thus, it is possible to have an experiment in the future to confirm the dynamics predicted by the current simulations.

1.4 Discussion

Theoretical framework for studying intermode couplings between normal modes in molecules was explored. In the case of H_2O, the Hamiltonian obtained using CVPT was used to simulate the population dynamics due to intermode coupling. The simulations can be extended to other simple molecules, although it will require much larger computational power, and the same Hamiltonian can also be used to study the dynamics of the correlations using any particular metric used in future experiments ($g^{(2)}$, entanglement entropy etc.). Such simulations would be give useful insight into experimental results obtained on studying quantum correlations in vibrational modes of molecules at room temperature.

2 Tunable Notch Filter

2.1 Introduction

Raman spectroscopy is a technique used to determine the vibrational eigen-frequencies of molecules. The Raman spectra of a molecule is considered to be a unique structural fingerprint. Notch filters are routinely used in Raman spectroscopy to reject elastically scattered and reflected light from the excitation laser and to simultaneously observe the Stokes and Anti-Stokes signals while filtering out the laser line. There is no commercially available broadband tunable notch filter (the ones used in experiments are made by combining short-pass and long-pass filters which also requires signals to be split and recombined, resulting in at least 50% loss). Having a high quality tunable notch filter is highly desirable for pulsed as well as CW Raman spectroscopy setups. Most importantly, being able to measure Stokes and anti-Stokes sidebands simultaneously allows both for "quantum thermometry" of the vibrational mode and for the investigation of the local photonic density of state to which the molecule is coupled. We plan to use such a filter to study correlations in molecules with a complex vibrational structure having multiple coupled modes as well as for CW spectroscopy of nanocavities. The aim was to design a tunable notch filter which surpasses the commercially available interference filters. Some figures of merit are:

- Broadband tunability (700-900 nm)
- High extinction ratio ($> 10^8$) which allows for better observation of Raman spectra. The extinction ratio can also be viewed as the exponential of the optical density at the desired wavelength.
- High throughput of the Raman signal.
- Collection of Stokes and Anti-Stokes signal with equal efficiency.
- Rejection bandwidth sufficiently small to allow measurement of Raman shifts down to $< 400 cm^{-1}$.

2.2 Methods

2.2.1 Simulation

Before being constructed, the design and performance of the notch filter was simulated using Zemax which is a powerful optical product design software. The central idea of the notch filter is to perform a fourier transform, which converts converts the frequency components into spatial components, then to recombine the light after spatially filtering out the unwanted frequency components. In other words, we want to disperse light, block the unwanted wavelengths and then recombine it. This can be acieved using a $4f-$geometry similar to what is routinely used for pulse shaping. An illustrative tutorial has been published by Chatel et. al. [6]

It is worth noting that in the Fourier plane (FP), all the spectral components are spatially separated and focused. Now, if we insert a physical block in the FP whose size is smaller than the spatial extent of the full spectral dispersion, then we would block only a few wavelengths and all other wavelengths in the beam would be re-collimated at the output. The design of the setup made in Zemax is shown below:

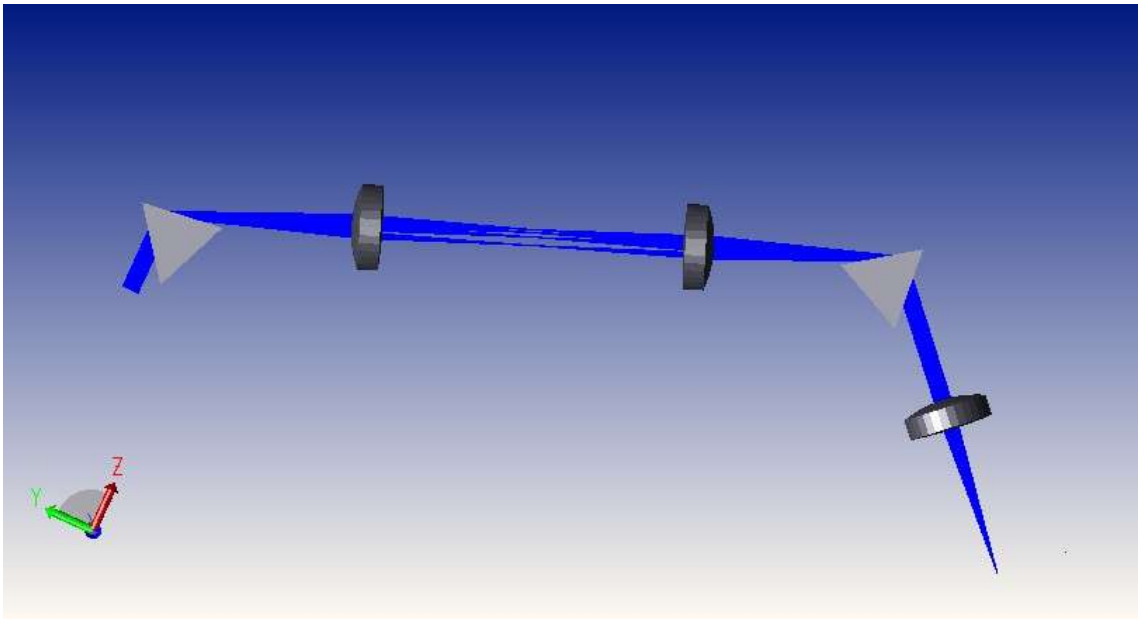

Figure 2.1 – The design of the notch filter simulated in Zemax is shown. The light is incident from the LHS and the $4f$ geometry is implemented using two prisms and two lenses. The third lens is used to check the overlap and collimation of light of different wavelengths by comparing the focal spots. The different wavelengths are clearly seen to be focused at different points in the intermediate focal plane.

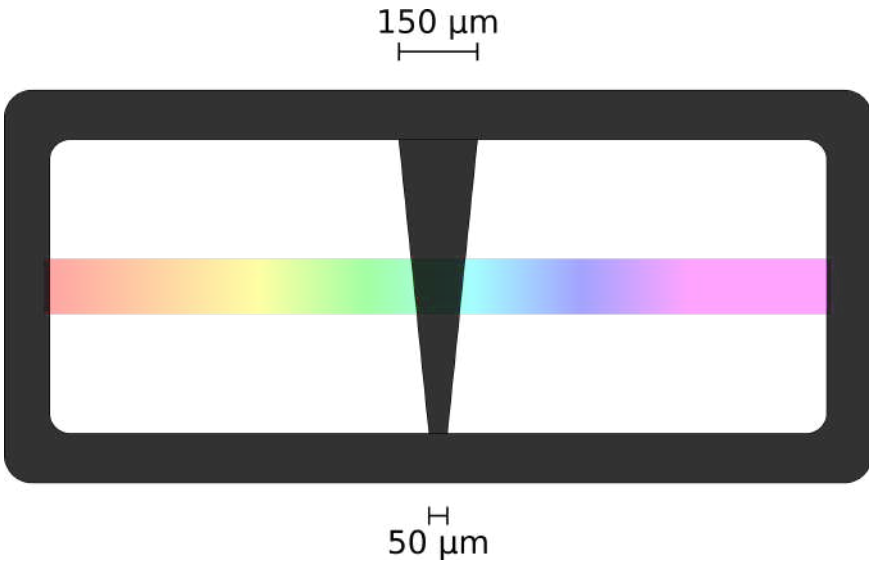

Figure 2.2 – The schematic representation of the notch is shown. It consists of a thin, tapered piece of metal placed in the FP

Many Zemax tools such as Spot diagram analysis, Physical Optics Propagation and Tolerancing were crucial in simulating and analysing the setup. A prism is used as the dispersing element because from analytical calculations it was found that it allows us to obtain a higher extinction ratio because refraction through glass does not greatly alter the beam profile.

2.2.2 Construction and Testing

Optical elements and light sources

The setup was constructed using standard optical elements (achromatic lenses, mirrors, prisms etc.) from Thorlabs.

Light sources: For aligning and characterising the notch filter, two main light sources were used:

- SpectraPhysics 3900S : Tunable (700 – 1050 nm) Ti:Sapphire laser.
- SuperK COMPACT supercontinuum source : spectrally broadened (450 – 2400 nm) pulsed laser (Pulse width $< 2ns$) which provides diffraction limited white laser light.

Optics and components:

- Prisms : Equilateral prisms of side length 25 mm and made of N-SF11 were used.
- Lenses : Achromatic lenses with focal length f = 50mm were used.

- Notch : The notch is mounted on a manual 3-axis stage which is used to align and adjust it in the intermediate focal plane.

Performance tests

The main tests conducted, whose results will be presented in the next section are :

- Test of extinction ratio.
- Test of control of notch width using tapered notch.
- Test of effect of defocussing on the notch spectrum.

2.3 Results

Test of extinction ratio

The extinction ratio is a measure of how effective the notch is at blocking the wavelength of choice. The extinction ratio was tested using the following setup:

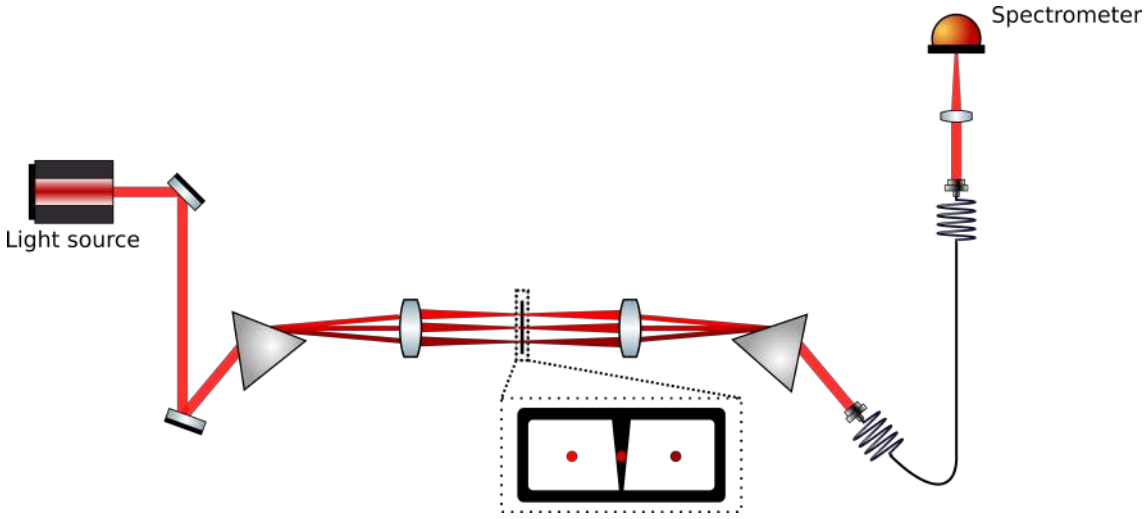

Figure 2.3 – A schematic of the setup used is shown. A CW laser was used as input to test the extinction ratio. For testing the tunability of the notch bandwidth as well as the effect of defocussing, the supercontinuum source was used in the same configuration.

The extinction ratio is calculated as follows:

- Compute integrated area under the attenuated laser peak before the filter is placed (a)
- Take the difference of the two values :
  - Area of the peak in the region of interest when notch is placed (b)
  - Area of peak in the region of interest when no beam is sent (and we couple only stray light) (c)
- Take the ratio of the two values ($\frac{a}{b-c}$)
- Correct for the factor contributed by the attenuation of the beam using ND filters at the output. This can be done by separately characterising the attenuation obtained using the particular configuration of ND filters. The attenuation of the ND filters was tested separately and the following value was obtained: **ND Attenuation** = $2.255 * 10^4$
- We consider the integration range to be $730 - 734$ nm and get the following values through numerical integration of data:
  - $a = 3.2294 * 10^5$
  - $b = 276042.623100$
  - $c = 276036.76053$

  Extinction Ratio = $\frac{a}{b-c} * ND\ Attenuation = 1.2421 * 10^9$

Test of spectral width

To test the spectral width of the notch filter, a SuperK Compact Supercontinuum Laser was used in the configuration shown in figure 2.3. Using the supercontinuum light source and a tapered notch, tests could be made of the change in notch width by moving in the direction of the tapering, as well as the spectral shape of the notch w.r.t defocussing of the notch for a fixed width.

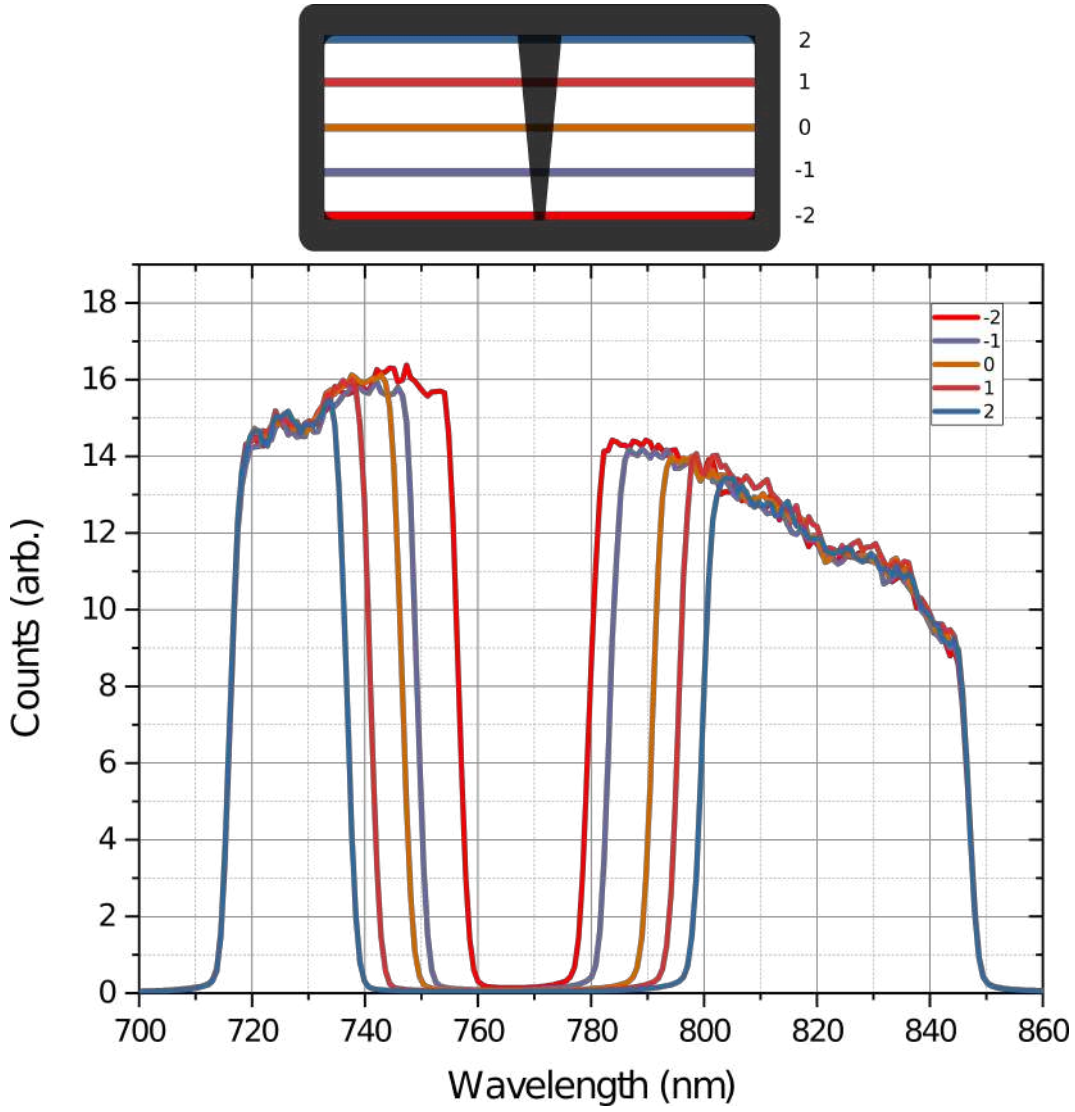

Figure 2.4 – The variation of the spectrum of the notch w.r.t the spatial width of the tapered notch is shown. The bands of different colours correspond to the different positions of the notch w.r.t the focus of the beam. The corresponding spectrum is plotted below using the same color. Thus, by using a tapered notch, the spectral bandwidth of the notch can be tuned easily

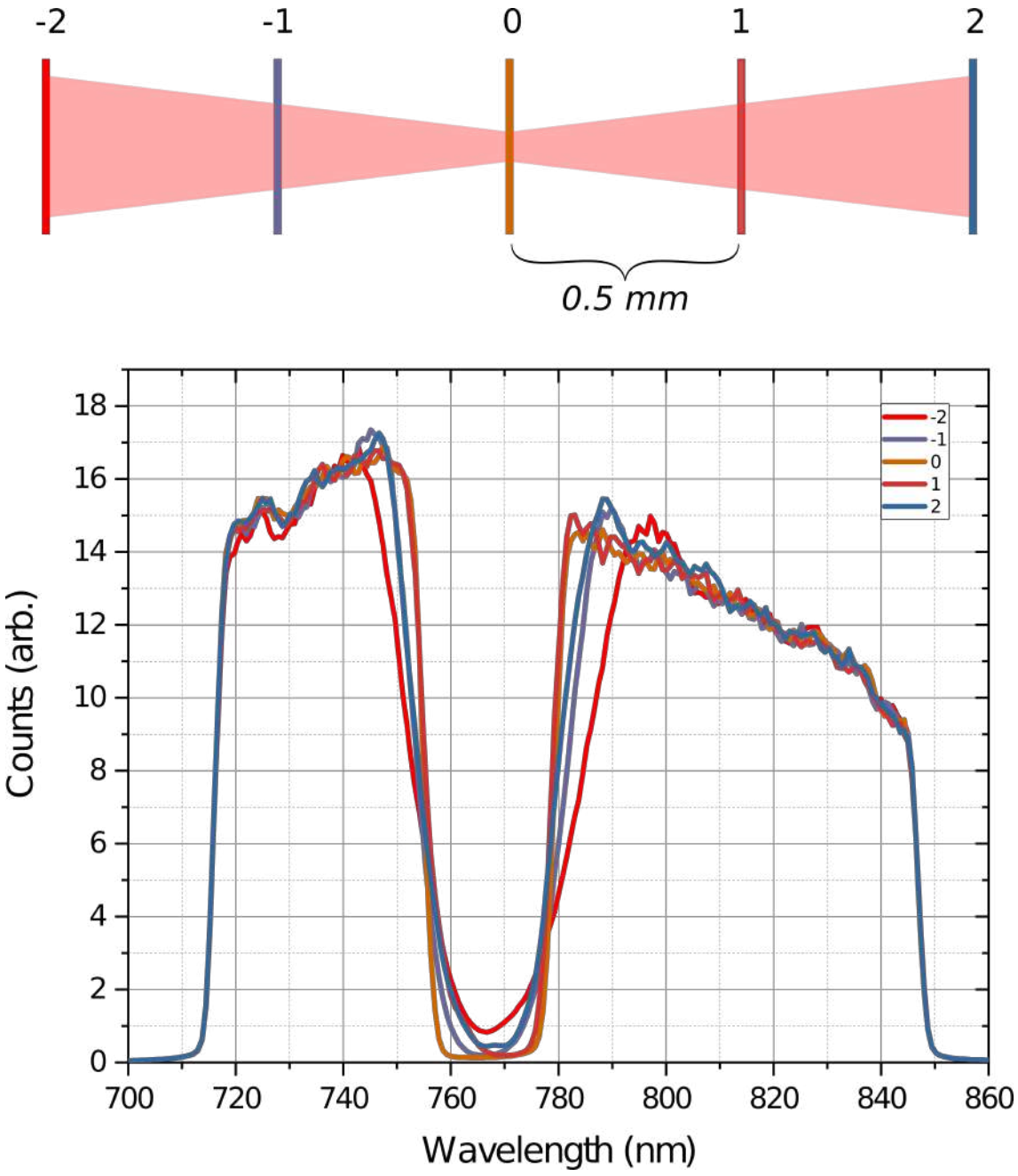

Figure 2.5 – The variation in the spectrum of the notch w.r.t defocussing is shown. The different colors of rectangles correspond to the different positions of the notch filter with the corresponding spectrum plotted below in the same color. We see that at the optimal position we get a flat notch spectrum as desired.

From the figure, we see that the tapered notch can be used to control the spectral width of the notch.

Spectroscopic test:
As explained before, we will use the tunable notch filter to eliminate the laser line in spectroscopic measurements. The setup used for the spectroscopic test along with the result obtained is shown below:

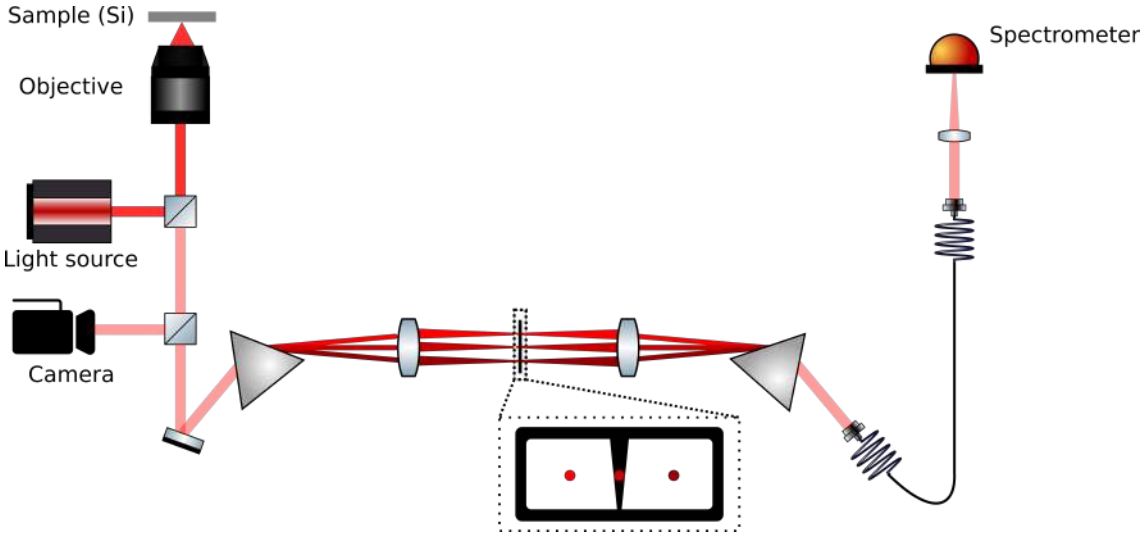

(a) Schematic diagram of the setup used to test the notch filter using a Silicon sample is shown.

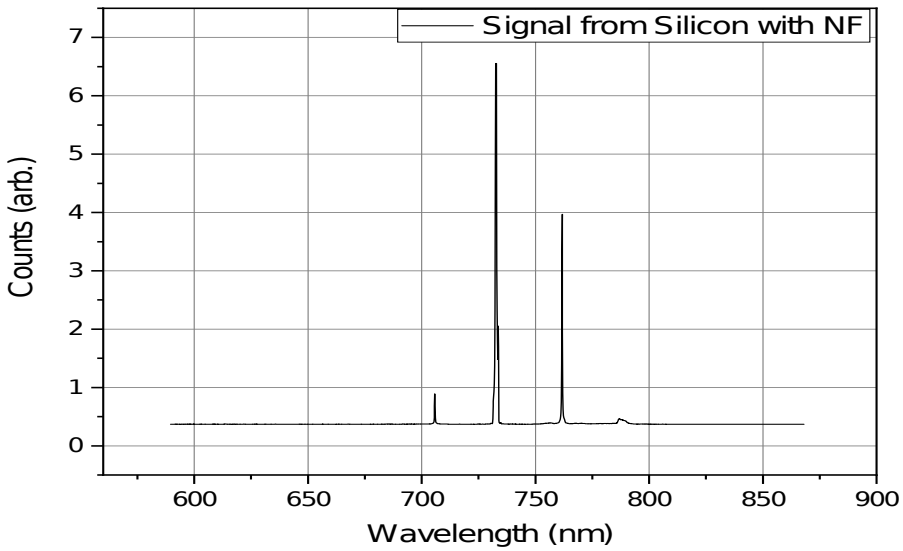

(b) The spectrum of obtained while testing the notch filter using Si sample is shown. The Stokes and Anti-Stokes peaks are seen clearly along with the residual laser light.

Thus we confirm that the notch filter can indeed be used to see the Stokes and Anti-Stokes sidebands in a single pass. This was previously possible only with very expensive triple-spectrometer setups.

2.4 Discussion

In light of the aims mentioned in the introduction, the main results achieved for the notch filter are :

- **Broadband tunability** : The notch filter can be tuned in a broadband range simply by moving the beam block in the FP. In fact, the filter can be recalibrated for a different wavelength range by reoptimising the design in Zemax. Additionally, we can also tune the spectral width of the notch using a tapered beam block.
- **High extinction ratio** : As shown in the methods section, we achieved an extinction ratio of $\approx 1.2 * 10^9$ which is higher than what can be achieved using commercial interference filters.
- **High throughput of the Raman signal** : The throughput of the setup is $\approx 64\%$. The reflective losses from the surfaces of the prism can be reduced by using prisms with an appropriate anti-reflection coating.
- **Collection of Stokes and Anti-Stokes signal** : Since we use a single pass without any signal splitting, we maximise the collection efficiency of the Raman signal.

The proposed design is extremely powerful in the sense that it can be easily modified to make a tunable notch (bandpass) with multiple regions of interest by having multiple tapered metal strips (slits).

3 Raman scattering and Photoluminescence from single nanocavities

3.1 Introduction

A single molecule picture was used in the previously presented molecular simulations. However, the experiments currently carried out in the group explore quantum correlations at room temperature in bulk materials. One of the visions for the future is to do such experiments at the single-molecule level. Experimentally, this can be done by placing the molecules in a nanocavity which enhances the light-matter interactions and enables the study of spectroscopic properties at the single molecule level. In direction of this goal, a microscopy setup for nanocavities was constructed. The aim of this setup is to integrate bright-field imaging, dark field imaging and observing spectra after laser excitation at multiple different wavelengths. We will begin by a brief schematic of the setup, followed by further details on each of the probed phenomenon. After this, some results will be presented.

3.2 Theory

3.2.1 Plasmonics and NPOM system

Metallic nano-structures are important in the field of photonics because they support localised surface plasmons (LSPs) which are able to strongly confine light into sub-wavelength volumes. The intense electric fields of the confined light lead to enhancement of many optical effects such as photoluminescence (PL), surface enhanced Raman scattering (SERS) and other non-linear processes (four-wave mixing etc.). In the field of nano-fabrication, not only have Nano-particles of many different shapes such as spheres, cubes and rods been fabricated, but assemblies of such nano-particles such as dimers and trimers are also made. An assembly of multiple nano-particles allows for the formation of a narrow gap which can hold some material of interest as well as enhance light-matter interaction due to strong field confinement.

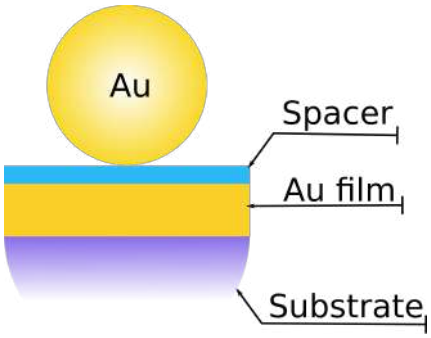

Figure 3.1 – Basic schematic of NPoM system

The plasmonic nano-cavity formed by a nanoparticle closely spaced from a metal film (as shown schematically for gold in the figure above) is our system of choice to perform plasmon enhanced spectroscopy. Thanks to the advancements in techniques for thin film deposition, spacer fabrication and nanoparticle fabrication, the Nano-Particle on Mirror (NPoM) platform allows for the tunability of plasmonic properties. The samples used in this study are shown below :

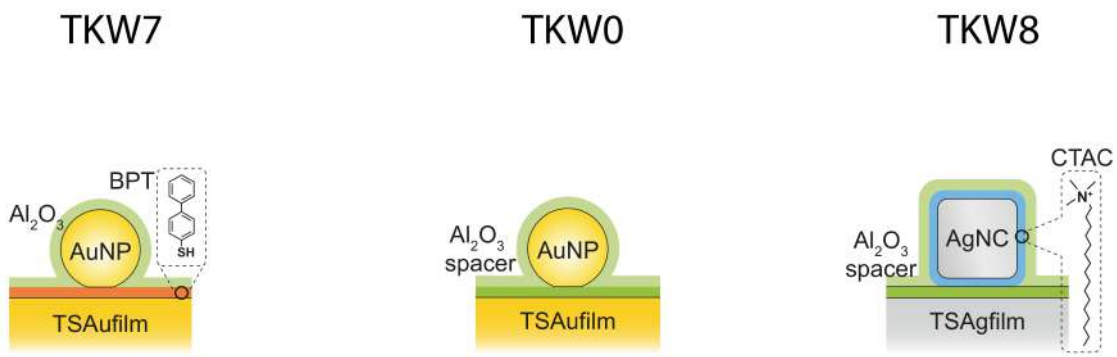

Figure 3.2 – 2D schematic of the tested NPoM systems

3.2.2 Photoluminescence

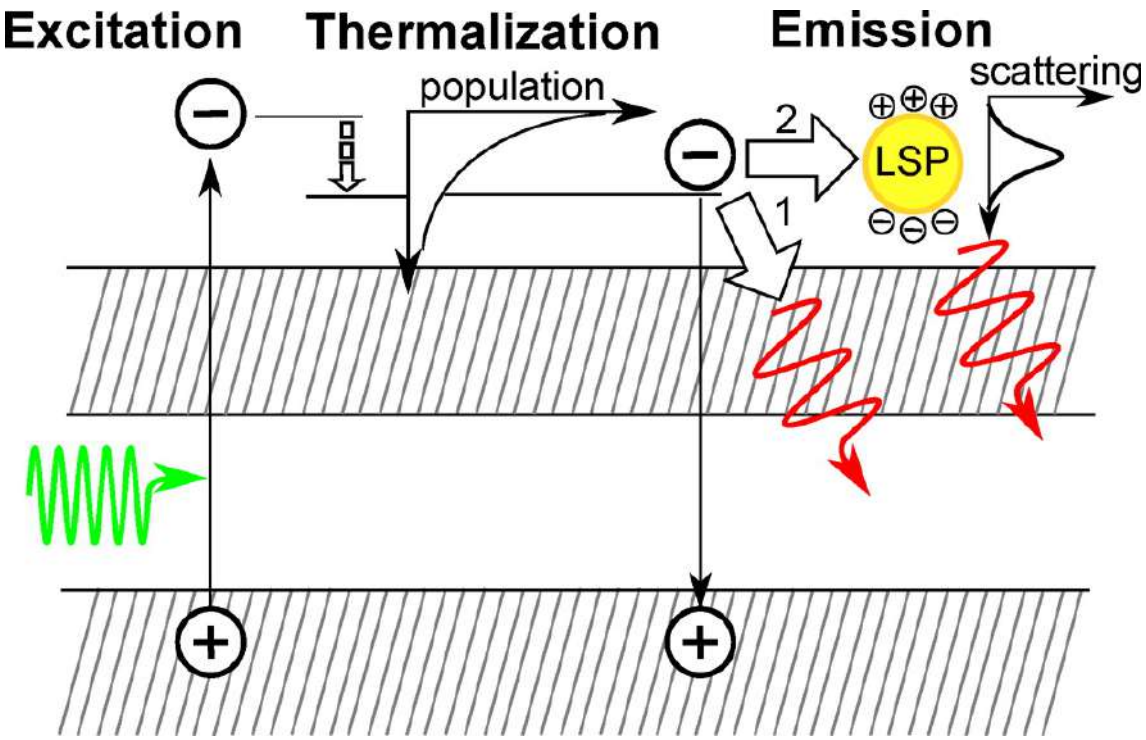

Figure 3.3 – Schematic for the mechanism of photoluminescence from gold is shown. Taken from ACS Photonics 2015, 2, 3, 432-438

Photoluminescence (PL) refers to the radiative decay process of photoexcited electrons and holes. It can be viewed as a three-step process consisting of electron-hole pair excitation, thermalisation (which leads to a broad range of electron energies and hence a broad spectral peak) followed by relaxation through direct radiative recombination or through the excitation of a localised surface plasmon (LSP) which subsequently decays radiatively (contributing to PL). An inuitive model can be built on this understanding. [7] For a plane metal film, in which there is no plasmonic relaxation pathway, the PL intensity can be written as :

$$I_{\mathrm{PL}}^{\mathrm{fim}}(\omega_{ex},\omega,\mathbf{r}) = U(\omega_{ex},\mathbf{r})\, f(\omega_{ex},\omega)\, \eta_0$$

$\omega \rightarrow$ Angular frequency

$\omega_{ex} \rightarrow$ Excitation frequency

$U = \frac{1}{2}\omega_{ex}\epsilon_0\epsilon''(\omega_{ex})|\mathbf{E}(\omega_{ex},\mathbf{r})|^2 \rightarrow$ Rate of excitation of electron-hole pairs

$\epsilon'' \rightarrow$ the imaginary part of the relative permitivity of the metal

$\mathbf{E}(\omega_{ex},\mathbf{r}) \rightarrow$ local electric field intensity

$f \rightarrow$ Probability density distribution of electron-hole pairs

$\eta_0 \rightarrow$ Quantum yield($\sim 10^{-10}$)

f has the property that $\int_0^{\omega_{ex}} f(\omega_{ex},\omega) = 1$ which gives the correct PL normalisation. Now, in the case of a metal nanoparticle, we have the additional relaxation path through the formation of a LSP. This is modelled by the probability $P(\omega,\mathbf{r})$. Thus, the PL intensity can be written as :

$$\begin{aligned} I_{\mathrm{PL}}^{\mathrm{ns}}(\omega_{\mathrm{ex}},\omega,\mathbf{r}) =& U(\omega_{\mathrm{ex}},\mathbf{r})\, f(\omega_{\mathrm{ex}},\omega)\left[\eta_0(1-P(\omega,\mathbf{r}))\right. \\ &\left.+P(\omega,\mathbf{r})\eta_{\mathrm{lsp}}\right] \qquad \text{where the last step is valid because } \eta_{lsp} >> \\ \approx& U(\omega_{\mathrm{ex}},\mathbf{r})\, f(\omega_{\mathrm{ex}},\omega)\left[\eta_0 + P(\omega,\mathbf{r})\eta_{\mathrm{lsp}}\right] \end{aligned}$$

η_0 since $\eta_{lsp} > 0.1$ for particles greater than $0.1nm$. $P(\omega,\mathbf{r})$ is proportional to the local density of states of the LSP. Thus, the probability of LSP excitation can be approximated by the local field enhancement at resonance:

$$P(\omega,\mathbf{r}) = \beta\frac{\left|\mathbf{E}\left(\omega_{\mathrm{lsp}},\mathbf{r}\right)\right|^2}{E_0^2}N(\omega)$$

$\beta \rightarrow$ Proportionality factor

$\mathbf{E} \rightarrow$ Electric field of LSP mode

$N(\omega) \rightarrow$ Normalisation factor

$N(\omega)$ is a function such that $N(\omega_{lsp}) = 1$ and decreases for frequencies away from resonance. This accounts for the fact that the probability of LSP excitation must decrease away from resonance. By dividing the intensities of the PL intesity of the film and nanoparticle, integrating them over the respective volumes and accounting for all LSPs (indexed by i) found in the system, the enhancement factor for PL can be calculated:

$$\mathrm{EF}(\omega_{\mathrm{ex}},\omega) = \frac{Q_{\mathrm{ns}}}{Q_{\mathrm{flm}}}\left[1 + \frac{1}{\eta_0}\sum_i \beta^{(i)}\eta_{\mathrm{lsp}}^{(i)}S^{(i)}N^{(i)}\right]$$

where $Q_i(\omega_{ex}) = \int_{metal} \mathrm{U}(\omega_{ew}\mathbf{r})\,\mathrm{d}V$ is the power absorbed by the film and S is defined as:

$$S\left(\omega_{ex},\omega_{lsp}\right) = \frac{1}{E_0^2 Q_{ns}} \int_{ns} U(\omega_{ex},\mathbf{r}) \left|\mathbf{E}\left(\omega_{lsp},\mathbf{r}\right)\right|^2 \mathrm{d}V$$

and it defines the mode overlap between the excitation and LSP mode.

3.2.3 Surface Enhanced Raman Scattering

Inelastic light scattering in molecular systems can be studied using Raman spectroscopy. Although the scattering cross section of molecules is extremely low ($\approx 10^{10}$ times smaller than the absorbtion cross section for fluorescence), the signal is seen to be greatly enhanced. The enhancement is attributed to the strong field localisation due to LSP excitation as well as chemical enhancement due to charge transfer between metal and molecules.

SERS from molecules in plasmonic cavities can be explained using principles of optomechanics where the plasmons make an optical cavity with a sub-wavelength mode volume which is coupled to the vibrations of the molecular species placed within the cavity [8] [9]. In the optomechanics description, the interaction between the vibrational modes and photons in the plasmonic cavity is described by the interaction Hamiltonian :

$$H_{\mathrm{I}} = -\frac{1}{2}\hat{\mathbf{p}}(t)\cdot\hat{\mathbf{E}}(\mathbf{r}_{\mathrm{m}},t)$$

$\hat{\mathbf{p}}(t)$ →molecular polarisation

$\hat{\mathbf{E}}(\mathbf{r}_{\mathrm{m}},t)$ →Electric field

$\mathbf{r}_{\mathrm{m}}$ →molecule's position

for a localised plasmon resonance with a lorentzian lineshape, the electric field can be written as :

$$\hat{\mathbf{E}}(\mathbf{r},t) = \mathbf{u}_{\mathrm{E}}\sqrt{\frac{\hbar\omega_{\mathrm{c}}}{2V\varepsilon_0\varepsilon}}\left[\hat{a}(t)\,u(\mathbf{r}) + \hat{a}^{\dagger}(t)\,u^{*}(\mathbf{r})\right]$$

ω_c →Center frequency of plasmon resonance

V →Effective mode volume

$\mathbf{u}_{\mathrm{E}}$ →Unit vector indicating polarisation

$u(\mathbf{r})$ →Gives spatial variation of electrical field

$\varepsilon_0\varepsilon$ →Permittivity of surrounding medium

$\hat{a}, \hat{a}^{\dagger}$ →The bosonic annihilation and creation operators

The electric field induces the molecular polarisation according to:

$$\hat{\mathbf{p}}(t) = (L_{\mathrm{m}})^{1/4}\,\alpha_{\mathrm{L}}(Q_{\mathrm{k}})\,\hat{\mathbf{E}}(\mathbf{r}_{\mathrm{m}},t)$$

$\alpha_{\mathrm{L}}(Q_{\mathrm{k}})$ →polarizability, which is a function of the normal coordinates

$(L_{\mathrm{m}})^{1/4} = (\varepsilon+2)/3$ →Electromagnetic local field correction

Expanding the molecular polarizability around the equilibrium configuration :

$$\alpha_{\mathrm{L}}(Q_{\mathrm{k}}) = \alpha_{\mathrm{L}}(0) + \left(\frac{\partial\alpha_{\mathrm{L}}}{\partial Q_{\mathrm{k}}}\right)_{Q_{\mathrm{k}}=0} Q_{\mathrm{k}} + \ldots$$

$\alpha_{\mathrm{L}}(0)$ describes the elastic scattering from the molecular vibrations (taken to be 0) and the second term describes the Raman scattering and is a function of $R_{\mathrm{k}} = (\partial\alpha_{\mathrm{L}}/\partial Q_{\mathrm{k}})_{Q_{\mathrm{k}}=0}$ and the zero point amplitude $Q_{\mathrm{k}}^0 = \sqrt{h/(2\omega_{\mathrm{m}})}$. In the 1D model, the potential energy of the molecule can be approximated as a shifted harmonic oscillator. Thus, the vibrational levels can be written in terms of creation and annihilation operators as :

$$\hat{Q}_k = Q_k^0(\hat{b} + \hat{b}^\dagger)$$

$\hat{b}, \hat{b}^\dagger \rightarrow$ Phonon annihilation and creation operators

Thus, the overall interaction Hamiltonian can be written as :

$$\hat{H}_{\mathrm{I}}(t) = -Q_{\mathrm{k}}^0 R_{\mathrm{k}} \frac{\hbar\omega_{\mathrm{c}}}{4\varepsilon_0\varepsilon V}\left(\hat{b} + \hat{b}^\dagger\right)\left[\hat{a}(t)\,u(\mathbf{r}_{\mathrm{m}}) + \hat{a}^\dagger(t)\,u^*(\mathbf{r}_{\mathrm{m}})\right]^2 (\mathbf{u}_{\mathrm{E}}\cdot\mathbf{u}_{\mathrm{k}})^2$$

The full Hamiltonian includes the energies of the cavity ($\hbar\omega_c$) and phonons ($\hbar\omega_m$) and a term corresponding to excitation by a laser of frequency ω_l and pumping rate Ω. Thus, the full Hamiltonian is :

$$\hat{H} = \hbar\omega_{\mathrm{m}}\hat{b}^\dagger\hat{b} + \hbar\omega_{\mathrm{c}}\hat{a}^\dagger\hat{a} - \hbar g_0\hat{a}^\dagger\hat{a}\left(\hat{b}^\dagger + \hat{b}\right) + \mathrm{i}\hbar\Omega\left(\hat{a}^\dagger \mathrm{e}^{-\mathrm{i}\omega_1 t} - \hat{a}\mathrm{e}^{\mathrm{i}\omega_1 t}\right)$$

$$g_0 = \frac{Q_{\mathrm{k}}^0 R_{\mathrm{k}}\omega_{\mathrm{c}}}{2\varepsilon_0\varepsilon V}\,|u(\mathbf{r}_{\mathrm{m}})|^2\,(\mathbf{u}_{\mathrm{E}}\cdot\mathbf{u}_{\mathrm{k}})^2 \rightarrow \text{Optomechanical coupling rate}$$

The interaction with environment is incorporated using the Master equation approach for the density matrix of the system:

$$\partial_t\rho = \frac{i}{\hbar}[\rho, \quad \hat{H}] + \frac{\kappa}{2}\mathscr{Q}_{\hat{a}}[\rho] + \frac{\left(n_b^{\mathrm{th}}+1\right)\gamma_{\mathrm{m}}}{2}\mathrm{D}_b[\rho] + \frac{n_{\mathrm{b}}^{\mathrm{th}}\gamma_{\mathrm{m}}}{2}\mathrm{D}_{\mathrm{b}}^\dagger[\rho]$$

$\frac{\kappa}{2}\mathscr{Q}_{\hat{a}}[\rho] \rightarrow$ describes the decay of plasmons

$\frac{\left(n_b^{\mathrm{th}}+1\right)\gamma_{\mathrm{m}}}{2}\mathrm{D}_b[\rho] \rightarrow$ Incoherent decay of vibrations due to thermal bath

$\frac{n_{\mathrm{b}}^{\mathrm{th}}\gamma_{\mathrm{m}}}{2}\mathrm{D}_{\mathrm{b}}^\dagger[\rho] \rightarrow$ Incoherent pumping of vibrations by thermal bath

In the quantum mechanical approach, the cavity is considered to be a bath coupled to the system of interest (phonons). Thus, a common approach is to solve the master equation for the reduced density matrix corresponding to the phonon modes. The cavity only modifies the transition rates between the vibrational states $\Gamma_{\pm}$, describing the creation and annihilation of

phonons.

$$\Gamma_{\pm} = \frac{g_0^2 |\alpha|^2 \kappa}{\left(\Delta' \pm \omega_{\mathrm{m}}\right)^2 + (\kappa/2)^2}$$

$g_0 \rightarrow$ Coupling rate to cavity

$\alpha \rightarrow$ Coherent state of the cavity

$\kappa \rightarrow$ Plasmon decay rate

$\Delta' - \Delta = -2g_0 \,\mathrm{Re}(\beta) \approx -2g_0^2 |\alpha|^2/\omega_{\mathrm{m}} \rightarrow$ Is negligible in most optomechanical platforms

$\Delta = \omega_{\mathrm{c}} - \omega_1 \rightarrow$ Laser detuning from cavity resonance

The emission spectra from the cavity is calculated as :

$$S(\omega) = \omega^4 \int_{-\infty}^{\infty} \mathrm{d}t \mathrm{e}^{-\mathrm{i}\omega t} \left\langle \hat{a}^{\dagger}(t)\hat{a}(0) \right\rangle_{\mathrm{ss}}$$

The ω^4 factor is added to account for characteristic dipolar emission. The peak intensity of the Stokes and Anti-Stokes emission is given by :

$$S(\omega_{\mathrm{aS}}) \propto \omega_{\mathrm{aS}}^4 \Gamma_- \frac{n_{\delta \mathrm{b}}}{\Gamma_{\mathrm{opt}} + \gamma_{\mathrm{m}}} \qquad S(\omega_{\mathrm{S}}) \propto \omega_{\mathrm{S}}^4 \Gamma_+ \frac{n_{\delta \mathrm{b}} + 1}{\Gamma_{\mathrm{opt}} + \gamma_{\mathrm{m}}}$$

$$\begin{aligned} \Gamma_{opt} &= \Gamma_- - \Gamma_+ \\ &= g_0^2 |\alpha|^2 \kappa \left(\frac{1}{(\Delta' - \omega_m)^2 + (\kappa/2)^2} - \frac{1}{(\Delta' + \omega_m)^2 + (\kappa/2)^2} \right) \end{aligned}$$

and the intensities integrated over the linewidths are :

$$\tilde{S}(\omega_{\mathrm{aS}}) \propto \omega_{\mathrm{aS}}^4 \Gamma_- n_{\delta \mathrm{b}} \qquad \tilde{S}(\omega_{\mathrm{S}}) \propto \omega_{\mathrm{S}}^4 \Gamma_+ \left(n_{\tilde{\mathrm{Bb}}} + 1 \right)$$

3.3 Methods

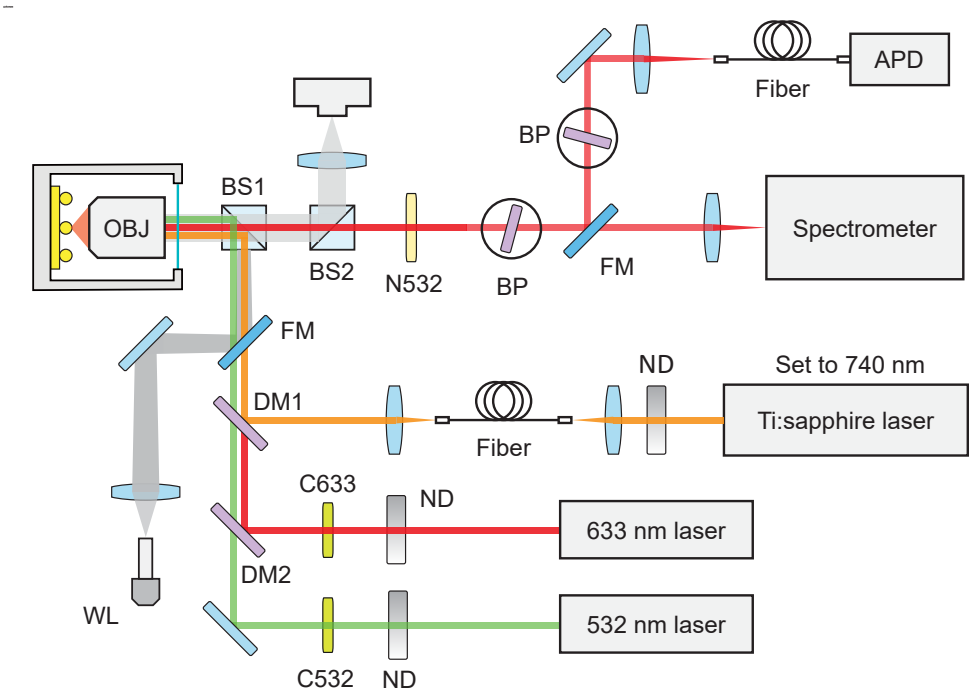

Figure 3.4 – The lightpath of the setup built around the AttoCube cryostat is shown. The white light sources are used to implement bright-field and dark-field illumination. Bright-field illumination aids in locating markers while dark-field illumination is used to locate nanoparticles. The paths of the various lasers used are overlapped using dichroic mirrors. The laser is then incident on a 8:92 (R:T) Pellicle Beamsplitter (BS1). The reflected laser light passes through the cryostat window and is focussed onto the sample by the objective, which also collects the light reflected from the sample. This includes the laser light as well as the signal of interest. Part of the reflected light is sent to an imaging camera (by BS2). The light transmitted by BS2 is then appropriately filtered using bandpass (BP) filters (to eliminate the laser light) and can be sent to a spectrometer (for spectral measurements) or to an APD (for fast acquisition measurements)

First, the techniques implemented in the setup will be introduced. This will be followed by a brief description of some of the equipment used in the experiment.

3.3.1 Bright-Field microscopy

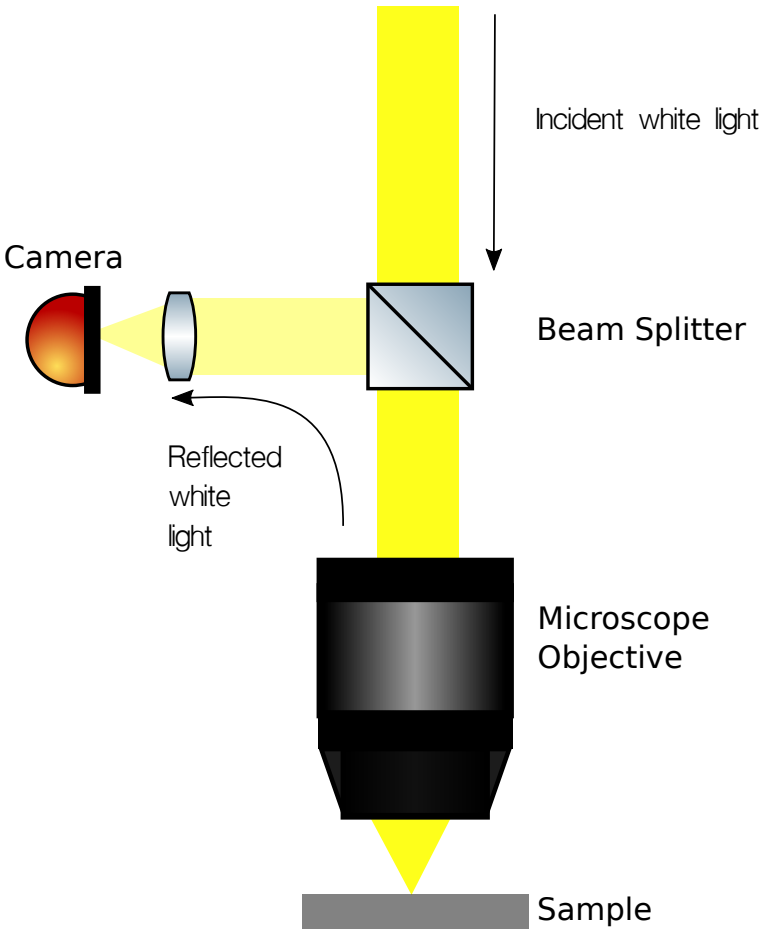

Figure 3.5 – Schematic diagram for implemented Bright-Field microscopy

This is a technique used to observe light reflected from a sample. White light from a lamp is guided through an objective onto the sample. The incident white light is focussed onto the back focal plane of the objective so that the transmitted light onto the sample is quasi-collimated. The reflected light from the sample is then collected and viewed using a CMOS camera whose focus is adjusted to ∞. This allows us to see the markers on the samples clearly.

3.3.2 Dark-Field microscopy

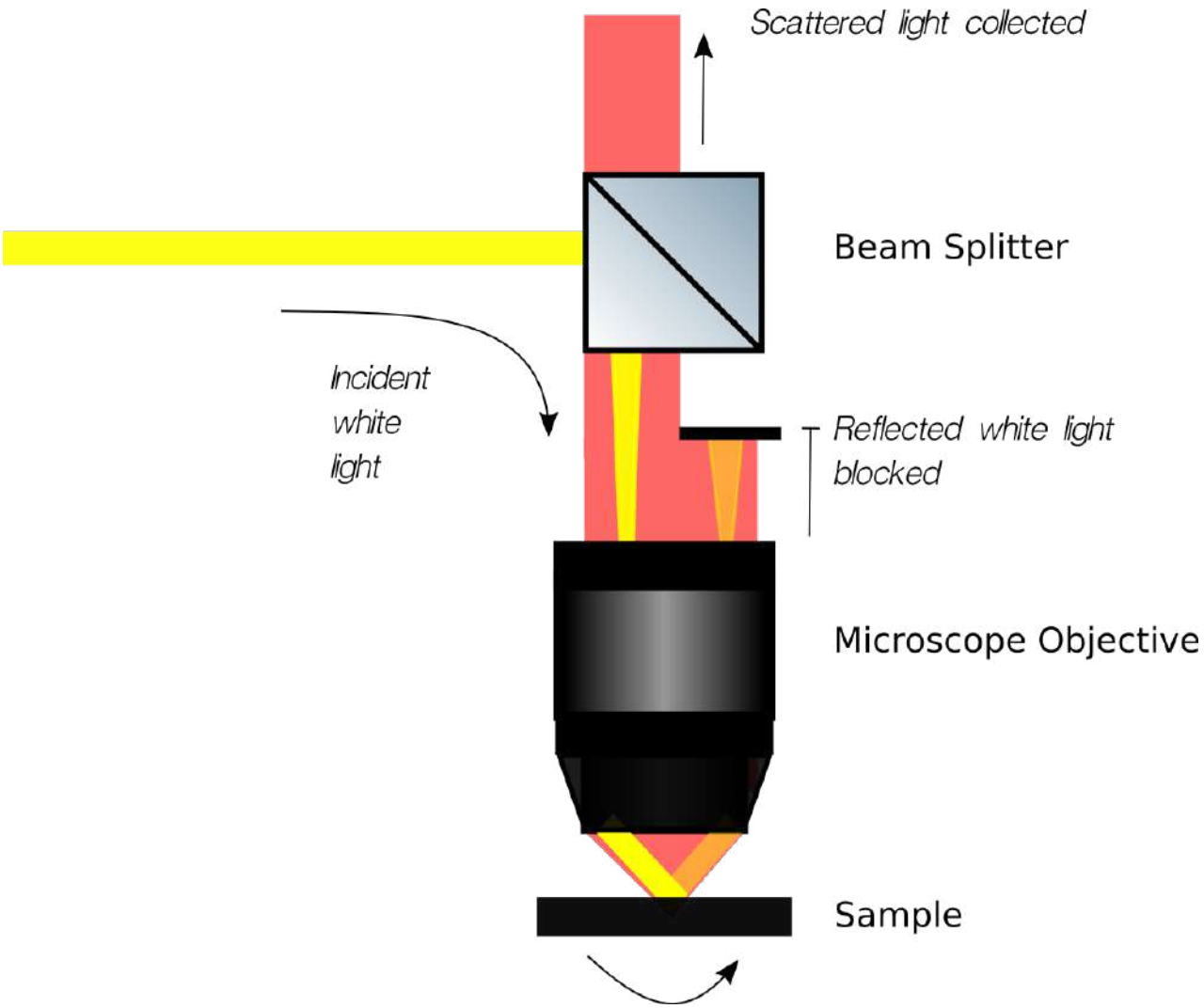

Figure 3.6 – Schematic diagram for implemented Dark-Field microscopy

Dark Field imaging is a technique used to observe the light scattered from the sample. The name is attributed to the fact that the background appears "Dark" as it is a plane surface which only reflects light specularly. The general idea is to exclude this specularly reflected component to collect only light scattered into other angles. The main advantage of Dark-Field microscopy is that it allows to image features beyond the diffraction limit ($\sim \lambda/d$). In our scheme, white light is first focussed onto the back focal plane of the objective on one side of the aperture. The specularly reflected light returning from the opposite end of the aperture is blocked and only light scattered by the sample in other angles is collected through the objective. This configuration is used in our setup because of the limitation imposed by the short working distance of the objective ($0.6mm$).

3.3.3 Laser excitation and signal collection

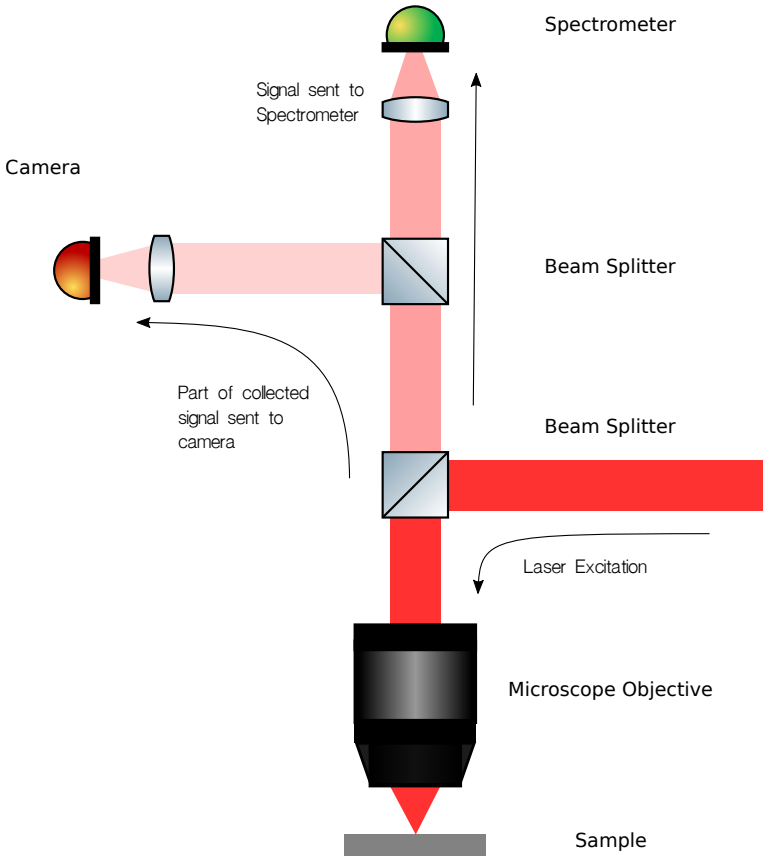

Figure 3.7 – Schematic diagram for laser spectroscopy

Collimated laser light is guided to the back aperture of the objective which then focusses it onto the sample. The reflected laser light, as well as signal emitted from the laser spot is then collected and collimated by the objective. Part of the reflected light is sent to the camera for alignment and focus adjustment. The remainder of the light is appropriately filtered and sent to the APD or spectrometer for measurement.

Following the summary of the implemented techniques, the important pieces of equipment used in the experiments will now be introduced:

3.3.4 Light sources

Tungsten Lamp

The light from a tungsten lamp is coupled into a fiber. The output lightis then collimated and used as a white light source for bright field imaging.
Power range $\approx 5mW$

SuperK COMPACT supercontinuum laser

The SuperK compact is a spectrally broadened (450 – 2400 nm) pulsed laser (Pulse width $< 2ns$) with a variable repetition rate ($1Hz - 20kHz$) which is used as a white light source for dark field illumination.

Power range $\approx 110mW$

SpectraPhysics 3900S

SpectraPhysics 3900S is a tunable ($700 - 1050nm$) Ti:Sapphire laser. This is used to perform SERS spectroscopy on NPOM systems.

Power range - $0.7 - 1.5W$

Thorlabs CPS532

The CPS 532 is a compact fixed wavelength ($532nm$) laser diode. This is used to perform PL measurements on NPOM systems.

Power range $\approx 4.5mW$

Velocity TLB 6300

The Velocity TLB 6300 laser is a tunable ($632.5 - 637nm$) external cavity laser diode. This is used to perform SERS spectroscopy on NPOM systems.

Power range $\approx 2 - 5mW$

Verdi V5

The Verdi V5 is a powerful ($5W$) green laser ($\lambda = 532nm$) which is often used as a pump laser. This is fiber coupled and used as a source for $532nm$ laser light for PL excitation.

Power range $\approx 5W$

3.3.5 AttoCube AttoDry 800

The AttoCube AttoDry 800 is a closed cycle cryostat wich is fully integrated into an optical table. This makes it ideal for use with optical setups in which the precise alignment of the path of incidence and collection is required. Some of the important features of the AttoCube AttoDry 800 are :

- Full integration with a (Newport) optical table. This allows for the optical setup to be constructed on the same table (as shown in the schematic) while also having a sample at low temperature.
- An apochromatic objective with high numerical aperture objective (0.8 NA) is integrated into the cryostat. This ensures high stability and enables stable long-time collection.
- Fully automated control over temperature from 3.8 K to 320 K.
- Extreme vibrational isolation. The residual vibrations on the cold plate in the cryostat are specified to be 2.6 nm peak-to-peak. This enables highly sensitive measurements to be made within the cryostat.

3.3.6 Andor Solis Kymera 193i Spectrometer

The Andor Kymera 193i is a highly customisable compact imaging spectrograph. The basic internal schematic can be seen in 3.4. We combine the Kymera with an Andor iDus (CCD camera. In the measurements presented, a 500 l/mm grating is used to disperse light in the spectrometer.

3.3.7 Single Photon Counting Module (SPCM)

The Excilitas SPCM-NIR-13 is a single photon counting module optimised for the near-infrared wavelength range (750 – 900 nm). Single photon counting modules work by having an avalanche photodiode operating in the Geiger mode. This is done by maintaining an APD above the breakdown voltage so that the arrival of a photon results in an avalanche. This results in a 'click' which is an electrical signal corresponding to the arrival of a photon to the SPCM. The avalanche is quenched by an active quenching circuit integrated with the APD. The Excilitas SPCM-NIR-13 has a single photon detecting efficiency (PDE) of ≈ 70% Some important figures of merit of the device are as follows :

Active area (dia)	Dark counts	PDE @ $780nm$	Max. count rate	Dead time	Pulse width
(μm)	(c/s)	(%)	(MHz)	(ns)	(ns)
180	250	70	37	22	10

3.3.8 IDQuantique ID900

The ID900 is a Time Controller with the following main features :

- Time-tagging
- On board time stamp processing (coincidence counts, filters etc.)
- Histogram generation based on time delay
- Pattern generation
- High speed (100 MHz) logic operation
- High speed (1GHz) counter

We use the high-speed time tagging feature of the ID900 to label the 'clicks' generated by the SPCM. The data is then post processed to look into the dynamics of blinking with higher time resolution.

3.4 Results

The setup was used to observe the PL (Photoluminescence) and SERS (Surface Enhanced Raman Scattering) from various NPOM (Nanoparticle on Mirror) systems. While making measurements, we came across the phenomena of PL blinking from NPOM systems and decided to investigate it in further detail.

3.4.1 Bright-Field

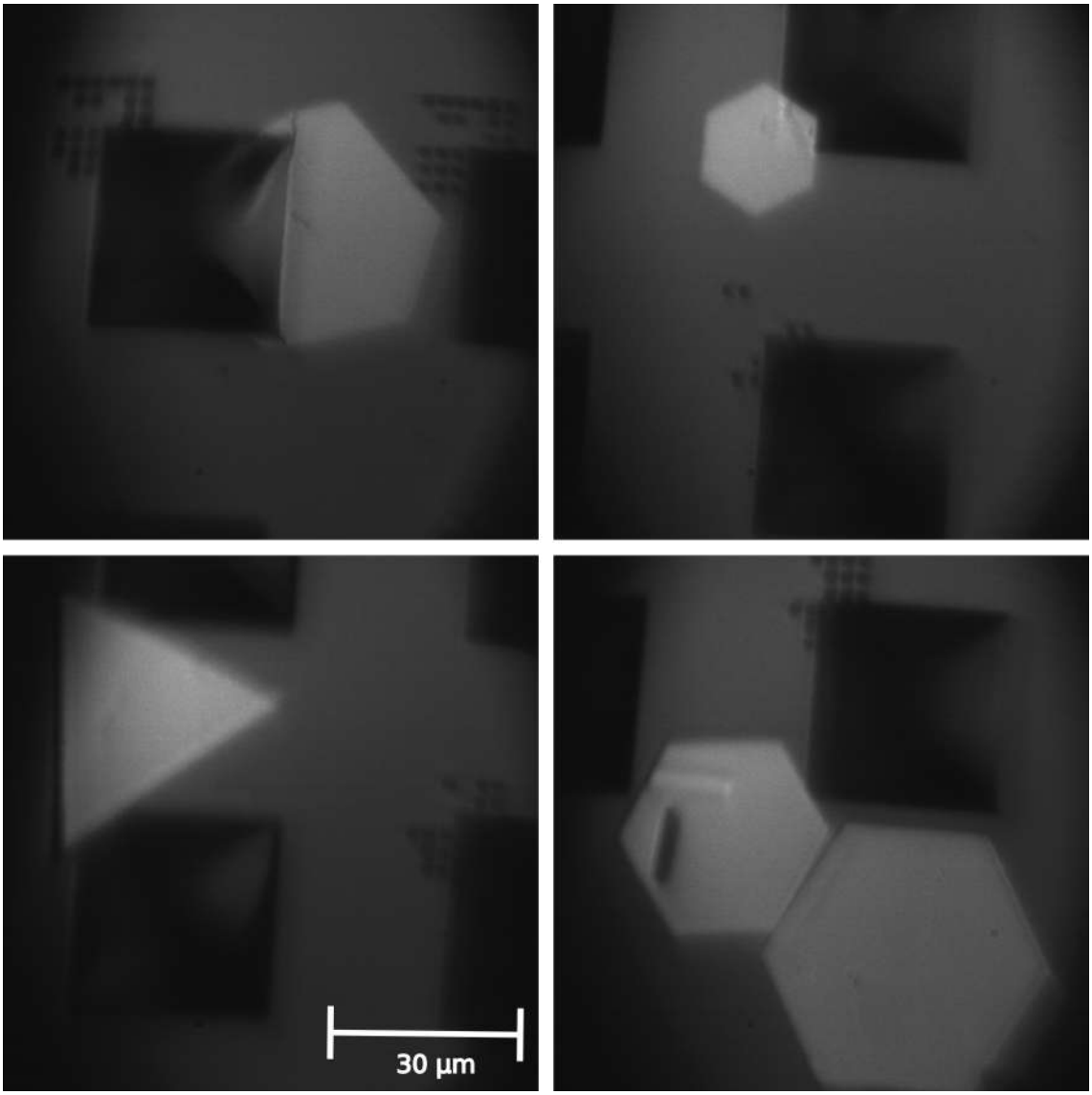

Figure 3.8 – Sample images captured in Bright-Field microscopy.

3.4.2 Dark-Field

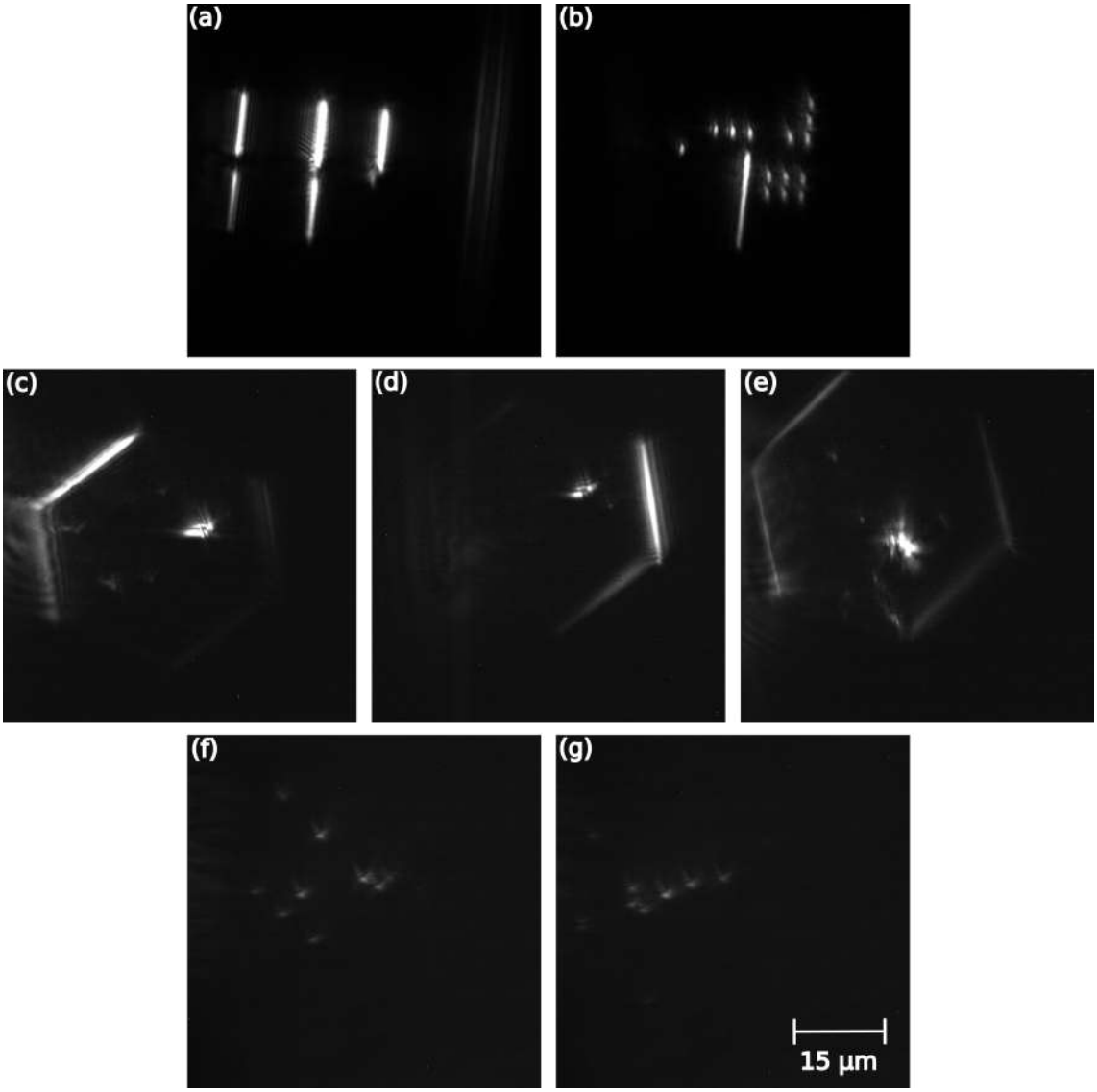

Figure 3.9 – Sample images captured in Dark-Field microscopy. We can clearly see all markers $(a) - (b)$, the microflakes $(c) - (e)$ as well as the nano-particles in $(f) - (g)$ and also on the micro-flakes. It is important to note that we don't see the donut shaped emission pattern from the nanoparticles, which is attributed to emission from the gap mode, because of the lower effective NA of our illumination geometry compared to what can be achieved in Dark-Field geometry using side illumination.

3.4.3 Photoluminescence (PL)

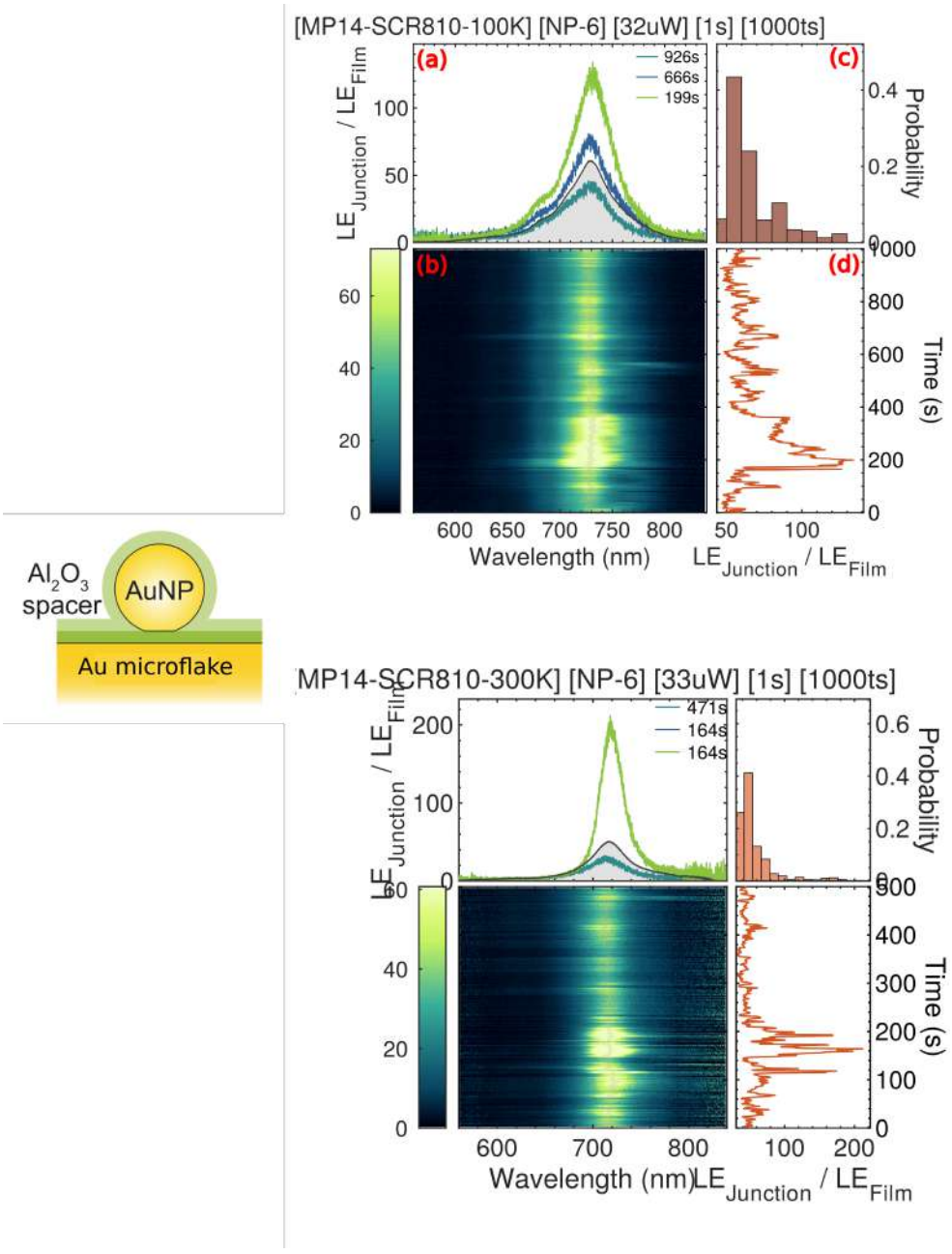

Figure 3.10 – Time series of the spectral data is shown. The sample temperature is $100K$ for the upper figure and $300K$ for the lower figure. We use a 532 nm laser for illumination. In each subfigure, (a) represents a few selected spectra of blinking events from the full time series spectrum (b). (c) represents the histogram of counts in which we see a clear tail representative of the blinking events. (d) shows the observed fluctuations of the peak intensity.

3.4.4 SERS+PL

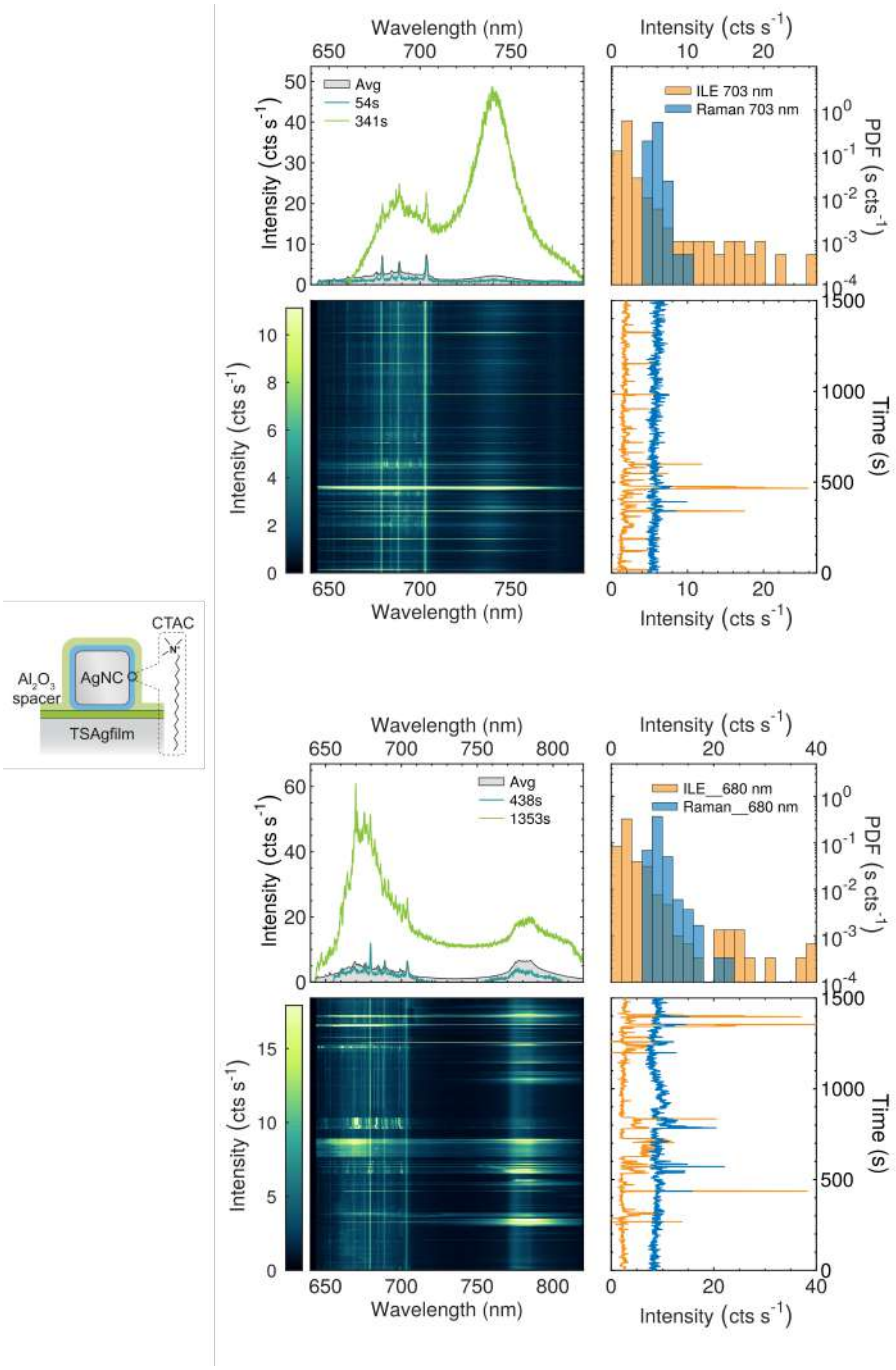

Figure 3.11 – Time series of the spectral data is shown. We use a 532 nm laser (for PL) as well as a 740 nm laser (for SERS) in illumination. The sample temperature is 290K for the upper figure and 4K for the lower figure. From the time series, we see that the PL and SERS blink independently. In these figures, 'LE' - Light emission and 'ILE' - Intrinsic light emission (PL).

From these measurements, in which the PL and SERS is monitored simultaneously, we see that the PL intensity blinks independent of the SERS signal.

3.4.5 Blinking SPCM measurement

In order to further resolve the timescale of the observed blinking phenomena, a SPCM was used in the collection path. The timestamps of the resulting clicks were recording using the ID900. Similar studies have been previously carried out for SERS emission [10]. Using the timestamps collected from the ID900, the time trace of the intensity of emission was plotted as a function of time. In some of these time traces, we do see strong blinking features which occur at timescales much faster than what we could resolve from the spectrometer ($\approx$ 1s). A few representative time series exhibiting blinking are shown below at two different resolutions ($1s$ and $1ms$ respectively) :

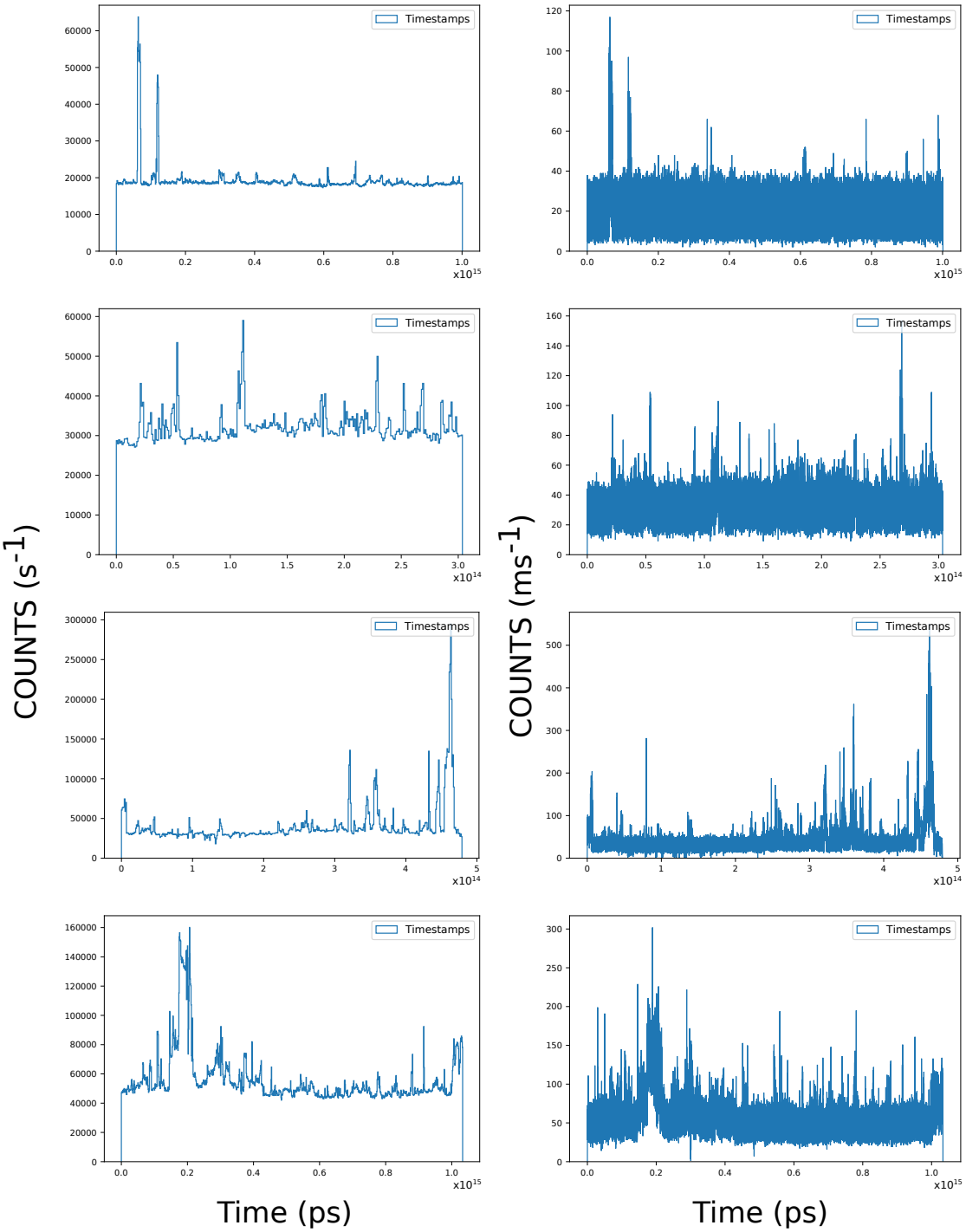

Figure 3.12 – A few representative time series are shown with 1s (left) and 1ms (right) time resolution. We clearly see that many blinking events appear to occur at the millisecond timescale.

To analyse the blinking data, we adopt the following methodology :

- **SPCM Noise analysis:** To characterize the noise due to the SPCM, we use a laser signal having constant power. This gives us a constant (I) number of counts per unit time with some noise. From the collected time series, we plot the standard deviation of the time series as a function of the mean number of counts. We then fit the data using a function of the form:

  $$\sigma_M(I) = \sqrt{(\sigma_L I)^2 + (\sigma_S \sqrt{I})^2 + \sigma_D^2}$$

  Here, The σ_D term corresponds to the dark noise, the σ_S term to the Shot noise (which scales as the square root of intensity) and the σ_L term to the laser noise. The data along with the fitted function is shown below:

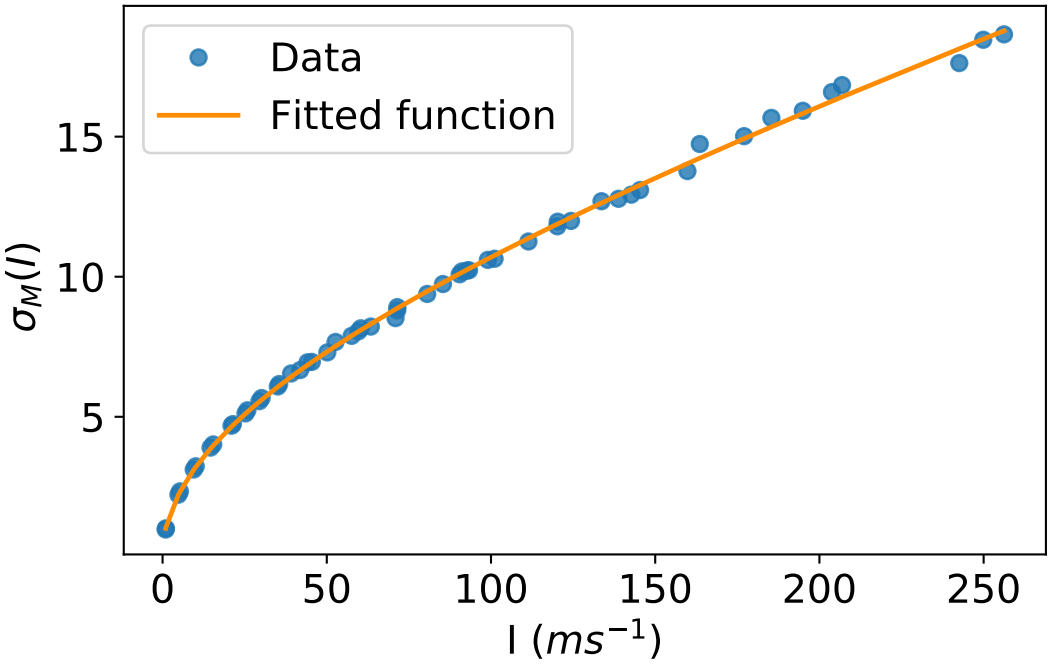

Figure 3.13 – The SPCM noise as a function of the mean count number is shown. The optimal parameters for the fit are $\sigma_L = 0.038$, $\sigma_S = 0.9969$ and $\sigma_D = 0.3089$.

- **Defining blinking threshold** : From the time series data containing blinking events, the baseline (I_{bas}) is extracted and the noise is fitted using a gaussian function of the form :

  $$exp[-(I - I_{bas})^2 / 2\sigma_M(I_{bas})^2]$$

  For a Gaussian distribution having mean μ and standard deviation σ, we know that $Pr(\mu - 3\sigma \leq X \leq \mu + 3\sigma) \approx 0.9973$. Thus we define the threshold for blinking as $I_{bas} +$

$3\sigma_M(I_{bas})$. Some representative graphs showing the histogram of counts above threshold are plotted below:

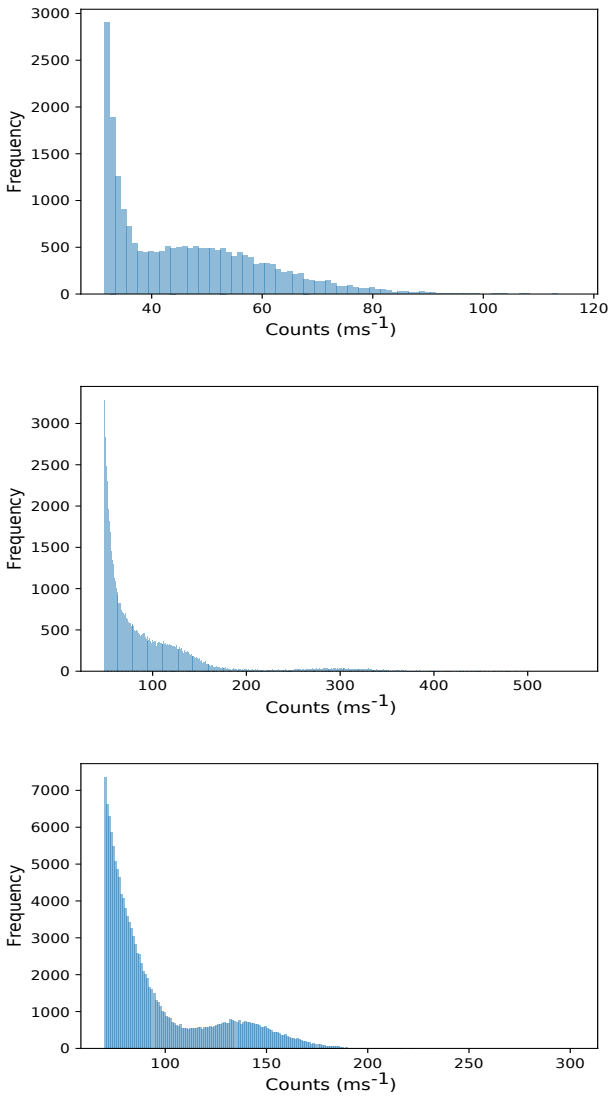

Figure 3.14 – The histogram of counts above threshold for a few time series is shown. We clearly see a deviation from the Gaussian tail expected from noise. The appearance of bumps indicates the presence of a a wide range of 'on' states.

Variation of blinking rate with laser power

Studying the power dependance of the plasmonic blinking would give us useful insight into the mechanism. To study the power dependance, the power of the (532 nm) laser was swept in the range $0.5\mu W - 100\mu W$ and the average blinking rate was computed. A blinking event is said to occur when the counts exceed the aforementioned threshold determined from the noise. A graph showing the result from one of the nanoparticles is shown below:

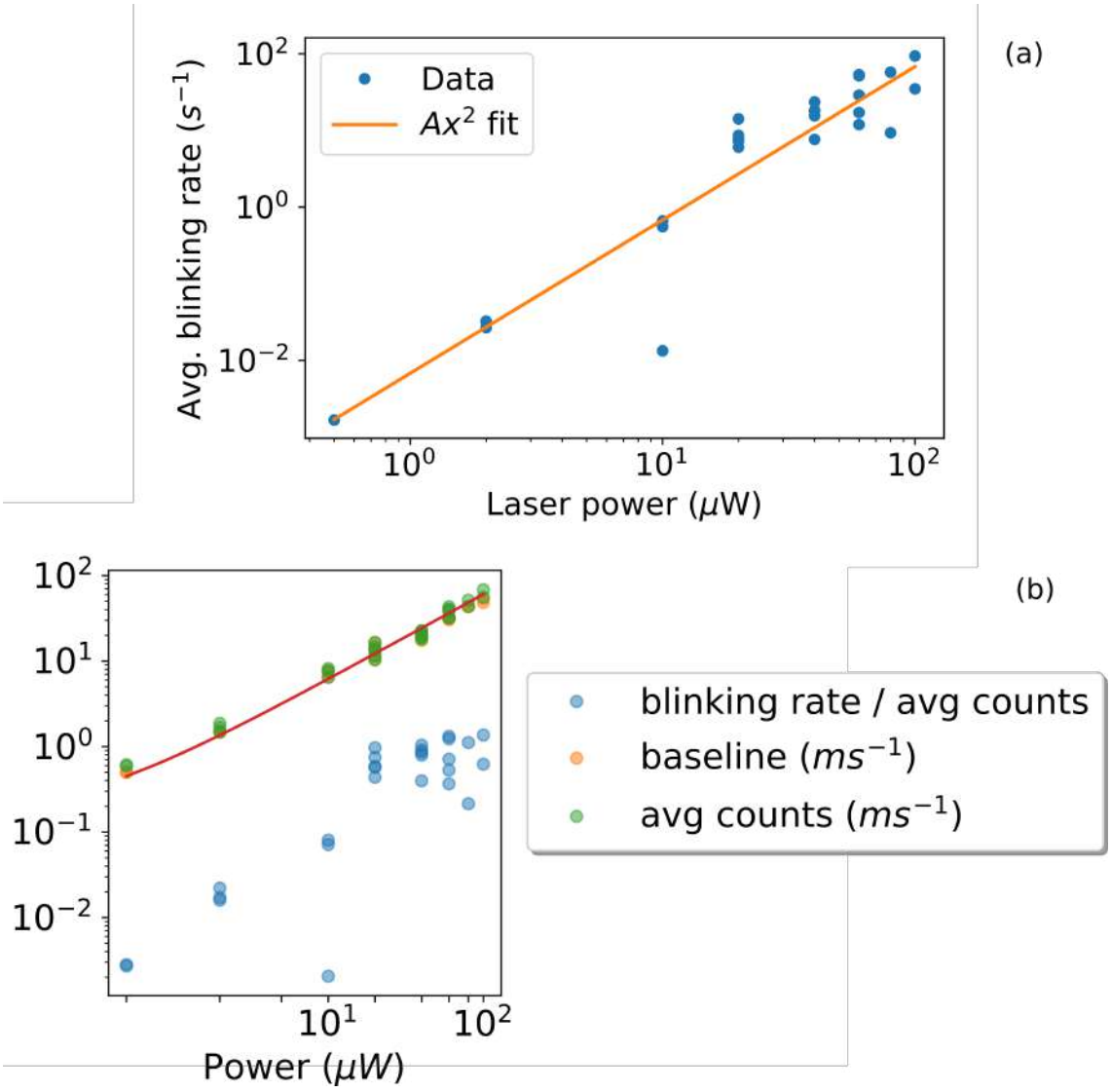

Figure 3.15 – In (*a*), the variation of the average blinking rate with power is shown. We see a clear quadratic scaling ($A = 0.00678$). The quadratic scaling may be due to the fact that the local defects leading to plasmonic blinking are optically driven through the field in the gap. In (*b*) we show the normalised blinking rate along with the average and baseline counts. We see that the Average and Baseline counts increase linearly ($y = 0.604x + 0.149$) with power while the normalised blinking rate appears to saturate at higher powers.

3.5 Discussion

In the multimodal cryogenic microscopy setup described, the Bright Field and Dark field microscopy techniques are used to locate the markers and the nanoparticles on the sample respectively. We have also integrated multiple lasers in the excitation path which allow us to study many different phenomena of interest in plasmonic nanocavities. The setup was assembled and used to study the metal-induced luminescence fluctuations. As described in the theory section, the broad photoluminescence emission originates from the excitation of electron hole pairs due to laser illumination (at 532 nm) and their subsequent direct recombination or indirect radiative decay mediated by a localised surface plasmon. We report the 'blinking' of this photoluminescence signal. Such blinking behaviour has been previously reported in systems of lower dimension wherein the quantum confinement plays a role in patterning the density of states [11–14].

The SERS signal from the plasmonic nanocavity is a sensitive probe of the near field enhancement inside the gap [15, 16]. We tune a second laser to 740 nm so that the Stokes signal from the BPT molecules in the spacer layer is resonant with the plasmonic mode (verified by dark field spectroscopy). The fact that we see the Photoluminescence signal blinking strongly while the variation of the Raman signal is within the measurement noise means that the blinking does not occur simply because of a change in the field enhancement of the cavity.

By operating at cryogenic temperatures, we verified that the blinking behaviour also persists at low temperature. Data taken at low temperature also allowed us to decouple the observed photoluminescence blinking from the formation of 'picocavities' which are attributed to atomic scale changes in the gap leading to extreme local field gradients and lead to appearance of new modes in the Raman spectrum with anomalous intensities [15, 16]. Hence, the blinking effect does not occur through the same mechanism as the one responsible for picocavity formation.

Together with other experiments carried out in the group, we have compelling evidence to ascribe the photoluminescence blinking to localised hotspots formed by the photoexcited hot-electrons [17]. This study instigates new questions into the mechanism of light emission from metals in nano-junctions and the understanding gained will be will be useful to make advances in the field of photocatalysis, photodetection and energy harvesting applications.

A Appendix

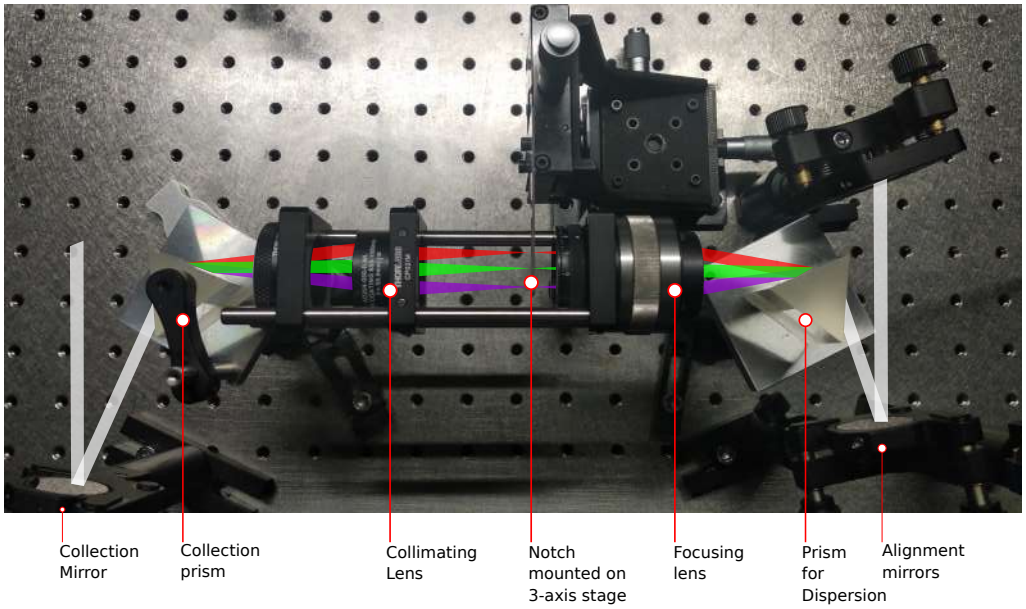

Figure A.1 – The picture of the Notch filter setup is shown along with representative light paths.

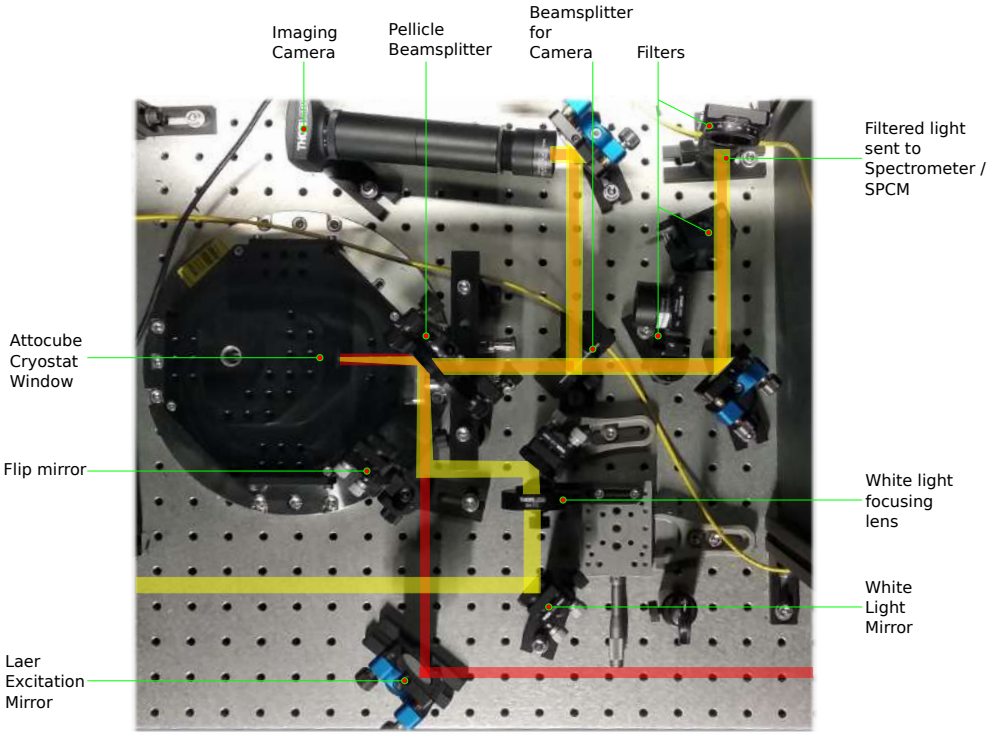

Figure A.2 – The picture of the Excitation and illumination path built near the AttoCube cryostat is shown along with representative light paths.

Bibliography

1. Velez, S. T. *et al.* Preparation and Decay of a Single Quantum of Vibration at Ambient Conditions. *Phys. Rev. X* **9,** 041007. https://link.aps.org/doi/10.1103/PhysRevX.9.041007 (4 Oct. 2019).
2. Martin Quack, F. M. *Handbook of High-resolution Spectroscopy* ISBN: 9780470066539 (Wiley Press, 2011).
3. Farantos, S. C., Schinke, R., Guo, H. & Joyeux, M. Energy Localization in Molecules, Bifurcation Phenomena, and Their Spectroscopic Signatures: The Global View. *Chemical Reviews* **109.** Publisher: American Chemical Society, 4248–4271. ISSN: 0009-2665. https://doi.org/10.1021/cr900069m (Sept. 2009).
4. Van Vleck, J. H. The Coupling of Angular Momentum Vectors in Molecules. *Rev. Mod. Phys.* **23,** 213–227. https://link.aps.org/doi/10.1103/RevModPhys.23.213 (3 July 1951).
5. Krasnoshchekov, S. V. & Stepanov, N. F. Polyad quantum numbers and multiple resonances in anharmonic vibrational studies of polyatomic molecules. *The Journal of Chemical Physics* **139,** 184101. eprint: https://doi.org/10.1063/1.4829143. https://doi.org/10.1063/1.4829143 (2013).
6. Monmayrant, A., Weber, S. & Chatel, B. A newcomer's guide to ultrashort pulse shaping and characterization. *Journal of Physics B: Atomic, Molecular and Optical Physics* **43,** 103001. https://doi.org/10.1088%2F0953-4075%2F43%2F10%2F103001 (May 2010).
7. Andersen, S. K. H., Pors, A. & Bozhevolnyi, S. I. Gold Photoluminescence Wavelength and Polarization Engineering. *ACS Photonics* **2,** 432–438. eprint: https://doi.org/10.1021/ph5004797. https://doi.org/10.1021/ph5004797 (2015).
8. Schmidt, M. K., Esteban, R., Benz, F., Baumberg, J. J. & Aizpurua, J. Linking classical and molecular optomechanics descriptions of SERS. *Faraday Discuss.* **205,** 31–65. http://dx.doi.org/10.1039/C7FD00145B (0 2017).
9. Roelli, P., Galland, C., Piro, N. & Kippenberg, T. J. Molecular cavity optomechanics as a theory of plasmon-enhanced Raman scattering. en. *Nature Nanotechnology* **11.** Number: 2 Publisher: Nature Publishing Group, 164–169. ISSN: 1748-3395. https://www.nature.com/articles/nnano.2015.264 (2020) (Feb. 2016).

10. Lindquist, N. C., Albuquerque, C. D. L. d., Sobral-Filho, R. G., Paci, I. & Brolo, A. G. High-speed imaging of surface-enhanced Raman scattering fluctuations from individual nanoparticles. en. *Nature Nanotechnology* **14.** Number: 10 Publisher: Nature Publishing Group, 981–987. ISSN: 1748-3395. https://www.nature.com/articles/s41565-019-0535-6 (2020) (Oct. 2019).

11. Nirmal, M. *et al.* Fluorescence Intermittency in Single Cadmium Selenide Nanocrystals. *Nature* **383,** 802–804 (Oct. 1996).

12. Bout, D. A. V. *et al.* Discrete Intensity Jumps and Intramolecular Electronic Energy Transfer in the Spectroscopy of Single Conjugated Polymer Molecules. *Science* **277,** 1074–1077 (Aug. 1997).

13. Hoogenboom, J. P., Hernando, J., van Dijk, E. M. H. P., van Hulst, N. F. & García-Parajó, M. F. Power-Law Blinking in the Fluorescence of Single Organic Molecules. *ChemPhysChem* **8,** 823–833 (2007).

14. Frantsuzov, P., Kuno, M., Jankó, B. & Marcus, R. A. Universal Emission Intermittency in Quantum Dots, Nanorods and Nanowires. *Nature Phys* **4,** 519–522 (July 2008).

15. Benz, F. *et al.* Single-Molecule Optomechanics in "Picocavities". *Science* **354,** 726–729. ISSN: 0036-8075, 1095-9203 (Nov. 2016).

16. Shin, H.-H. *et al.* Frequency-Domain Proof of the Existence of Atomic-Scale SERS Hot-Spots. *Nano Lett.* **18,** 262–271. ISSN: 1530-6984 (Jan. 2018).

17. Chen, W. *et al. Blinking of Purcell-enhanced continuum emission from Plasmonic Nanojunctions* In Preparation.